1-1-2016

# Thermo-Hydro-Mechanical Effects of Climate Change on Geotechnical Infrastructure

Joe Dylan Robinson

# Thermo-hydro-mechanical effects of climate change on geotechnical infrastructure

By

Joe Dylan Robinson

A Thesis
Submitted to the Faculty of
Mississippi State University
in Partial Fulfillment of the Requirements
for the Degree of Master of Science
in Civil Engineering
in the Department of Civil and Environmental Engineering

Mississippi State, Mississippi

May 2016

Thermo-hydro-mechanical effects of climate change on geotechnical infrastructure

By

Joe Dylan Robinson

Approved:

_____

Farshid Vahedifard
(Major Professor)

_____

George L. Mason Jr.
(Committee Member)

_____

John F. Peters
(Committee Member)

_____

Masoud Rais-Rohani
(Committee Member)

_____

James L. Martin
(Graduate Coordinator)

_____

Jason M. Keith
Dean
Bagley College of Engineering

Name: Joe Dylan Robinson

Date of Degree: May 6, 2016

Institution: Mississippi State University

Major Field: Civil Engineering

Major Professor: Dr. Farshid Vahedifard

Title of Study: Thermo-hydro-mechanical effects of climate change on geotechnical infrastructure

Pages in Study: 82

Candidate for Degree of Master of Science

The main goal of this research is to quantitatively assess the resilience and vulnerability of geotechnical infrastructure to extreme events under a changing climate. In the first part, pertinent facts and statistics regarding California's extreme drought and current status of its levees are presented. Weakening processes such as soil strength reduction, soil desiccation cracking, land subsidence and surface erosion, and oxidation of soil organic carbon are comprehensively evaluated to illustrate the devastating impacts that the California drought can have on earthen structures. In the second part, rainfall-triggered slope instabilities are analyzed using extreme precipitation estimates, derived using the historical stationary and a proposed future nonstationary approach. The extremes are integrated into a series of fully coupled 2D finite element simulations. The final part of this study investigates the impact of simultaneous variations in soil moisture and temperature changes in the California region on soil strength through a proposed thermo-hydro-mechanical framework.

ACKNOWLEDGEMENTS

I would like to express my deepest gratitude to my advisor, Dr. Farshid Vahedifard. Throughout the past two years I have learned that, with hard work on both the effective and efficient levels, there is absolutely nothing that cannot be accomplished. Thank you Dr. Farshid for providing me with guidance and financial support. I have thoroughly enjoyed working with you over the past two years.

I would like to also send a great thanks to my thesis committee: Drs. George L. Mason, John F. Peters, and Masoud Rais-Rohani for their infinite supply of comments and suggestions, kindness, and patience throughout the past 24 months. To Dr. Mason, for the support and guidance throughout several research projects. To Dr. Peters, for his theoretical insight and friendship. Last but not least, to Dr. Rais-Rohani, for his considerable amount of support and patience; without the later I would have not been able to effectively complete a technical paper.

I would also like to extend a huge thanks to my colleagues Clay, Firas, Kimia, Mohammad, Shahriar, and Syed. Each of whom have provided me with the best group of friends and research group that any graduate student could dream of.

Last but not certainly not least, I would like to send out massive thanks to my parents, Laurie and Randy, and sisters, Malauri and Morgan Robinson. For all of my life, the four of you have provided me with an endless supply of love and support. I would

most certainly not be where I am today without you all by my side. So again, I say thank you for the memories that we have shared and the support that you have provided.

TABLE OF CONTENTS

LIST OF TABLES

LIST OF FIGURES

# CHAPTER I

# INTRODUCTION

## Background

There is ample evidence that the earth's climate is changing due to anthropogenic activities, and the frequency and severity of recent mean and extreme environmental trends such as average surface temperature, drought cycles, intensity of extreme precipitation, global sea-level rise, and storm intensity are anticipated to worsen in a changing climate (e.g., USGCRP 2009; EEA 2012; NOAA 2013; NRC 2014). These climate trends unfavorably influence existing natural and engineered earthen structures by exposing them to thermo-hydro mechanical weakening processes such as soil strength reduction, drying and shrinkage, soil desiccation, microbial oxidation of soil organic matter, fluctuation in the ground water table, land and surface erosion, and highly dynamic pore pressure changes (e.g., Dunbar et al. 2004; Vicuña et al. 2006; O'Kelly 2008; Dyer et al. 2009; Port and Hoover 2011; Brooks et al. 2012; Bates and Lund 2013; ASCE 2015; Cappa et al. 2015). Further, the imposed impacts of the aforementioned climatic trends can lead to various modes of failure such as uplift, sliding, heaving, subsidence, piping, internal erosion, and slope instability (e.g., NRC 2008; Crozier 2010; Taylor et al. 2013; Vardon 2014). It is almost inevitable that recent climate trends such as drought are superimposed by other climatic extremes such as severe flooding and storm surges, which adds more complexity to an already challenging problem.

California is currently suffering from a multiyear extreme drought and the impacts of the drought are anticipated to worsen under a changing climate. The resilience of critical geotechnical infrastructure under extreme drought conditions is a major concern that is currently poorly understood. There is a crucial need to improve our understanding of the potential threats of drought on infrastructure and take subsequent actions in a timely manner to mitigate these threats and adapt our infrastructure to cope with future extreme events. The need is more pronounced for urban and non-urban earthen levees, since their functionality to protect dry land and water resources, respectively, is more critical during drought conditions (Vahedifard et al. 2015a). A significant number of California's levee systems is currently operating under a high failure risk condition, indicating that they are in danger of failing during an earthquake or flood event. Failure of these systems would essentially inundate agricultural lands and contaminate water supply systems for several months to several years as a result of seawater intrusion.

In addition to extreme drought conditions, increased rainfall intensity under a changing climate can also threaten the structural stability of critical geotechnical infrastructure such as natural and engineered earthen slopes. In fact, extreme rainfall due to climate change is recognized as one of the major causes of instabilities in natural and engineered earthen structures (e.g., NRC 2008). Rainfall-triggered slope instabilities are analyzed primarily using extreme precipitation estimates, derived using the so-called stationary assumption (i.e., statistics of extreme events will not vary significantly over a long period of time). However, extreme precipitation patterns have shown to vary substantially due to climate change and variability, leading to unprecedented changes in

statistics of extremes. Ignoring such an impact in the analysis of earthen structures can lead to a major underestimation in the intensity of rainfall that such slopes may experience over time. Thus, the impacts of future (projected) precipitation patterns on the short and long term behavior of geotechnical infrastructure such as natural and engineered earthen slopes is an emerging issue that deserves immediate attention.

## Objectives

The main objective of this research is to quantitatively assess the resilience and vulnerability of critical geotechnical infrastructure such as natural and engineered earthen structures to extreme events under a changing climate.

## Scope

The first goal of this research is to comprehensively discuss how California's protracted drought can further threaten the integrity of the already at-risk levee systems through the imposition of several thermo-hydro-mechanical weakening processes. To accomplish this task, pertinent facts and statistics regarding California's drought and current status of its levees are presented. Lessons from previous catastrophic levee failures and major damages which occurred under similar extreme events are discussed. Weakening processes such as soil strength reduction, soil desiccation cracking, land subsidence and surface erosion, and microbial oxidation of soil organic carbon are comprehensively evaluated to illustrate the devastating impacts that the ongoing California drought can have on earthen levees.

The second goal of this research is to quantitatively assess natural slope instabilities due to extreme precipitation events under climatic variations. To accomplish

this task, a nonstationary approach, applied to future climate model simulations, is adopted to project future precipitation extremes. Future precipitation estimates are obtained from the Coupled Model Intercomparison Project Phase 5 (CMIP5) simulations. Baseline (historical) and projected (future) precipitation extremes are obtained for a study area near Seattle, WA. Both baseline and projected precipitation patterns are integrated into a series of fully coupled 2D stress-unsaturated flow finite element simulations. The responses of the baseline and projected 2D finite element models at a 7-day rainfall duration obtained for a 50-year recurrence interval are compared in terms of factor of safety, displacements, matric suctions, and corresponding suction stresses.

The final goal of this research is to propose an innovative and conceptual thermo-hydro-mechanical framework to assess relationships between concurrent variations in soil temperature and moisture and consequently, reductions in soil strength under extreme events such as protracted drought due to a changing climate. The goal of this framework is to carefully understand the effects of the rate and variability of soil temperature and moisture changes under a changing climate on the short- and long-term thermo-hydro-mechanical properties (e.g., shear strength) of soil. This is accomplished through the use of satellite soil moisture and temperature data, along with pertinent soil properties, obtained for a study area in the Sacramento San Joaquin Delta (Delta), California.

CHAPTER II

# CAN PROTRACTED DROUGHT UNDERMINE THE STRUCTURAL INTEGRITY OF CALIFORNIA'S EARTHEN LEVEES?

## Introduction

The frequency and severity of California's drought are anticipated to worsen in a warming climate (Port and Hoover 2011). The Millennium Drought (1997-2009), that severely impacted the economy and environment in southeastern Australia (AghaKouchak et al. 2014a), is often considered as an archetype of an extreme event expected to occur in California. The Millennium Drought had a negative impact on river ecosystems, dry land and irrigated agriculture, and surface water storage in natural and engineered reservoirs (Van Dijk et al. 2013). The event led to significant reduction in production of water-intensive crops (e.g., rice and cotton) by up to 99%, resulting in over $4.5 billion in Federal Government drought assistance and investments in multi-billion dollar water infrastructure for improving preparedness and response (Van Dijk et al. 2013).

The 2012-2015 California drought has been one of the most extreme on record, characterized by low precipitation and high temperatures (Shukla et al. 2015; AghaKouchak et al., 2015). Figure 1a displays snapshots of drought conditions from 2012 to 2015 based on the Standardized Soil Moisture Index (SSI) (Hao et al. 2014). As can be seen in Figure 1a, the most severe drought on record occurred in May 2014 and

the drought continues to remain in a critical condition. The severity of drought is in part a result of the lack of snow pack, which affects the overall exploitable water supply throughout the state. As Figure 1a indicates, there is also a shortage of soil moisture, which comes in addition to the water shortages caused by lack of snow packs. Figures 1b and 1c show the four-year average precipitation and temperature, respectively. The concurrent extreme low precipitation (Figure 1b) and high temperature (Figure 1c) was estimated to be a 200-year extreme event (AghaKouchak et al. 2014b).

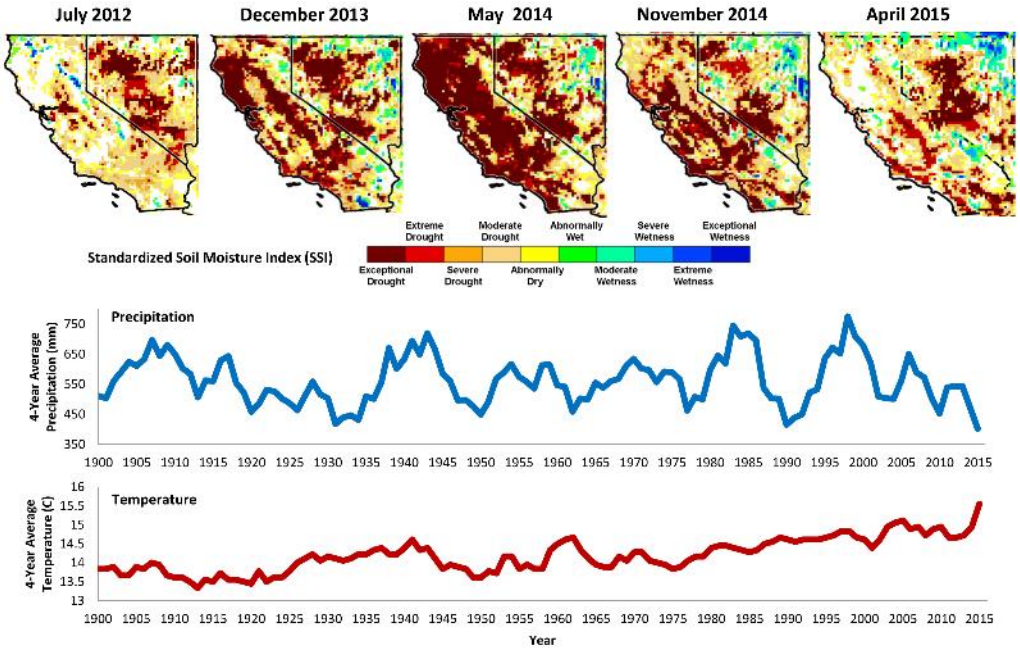


Figure 1 (a) Snapshots of drought based on Standardized Soil Moisture Index (SSI); (b) Four-year average precipitation (mm); and (c) Four-year average temperature (°C).

This chapter intends to stimulate discussions among the geotechnical engineering community regarding the effects of California's prolonged drought on levees in the Central Valley and Sacramento-San Joaquin Delta (Delta). There is a clear gap in the

state of our knowledge in terms of structural-scale assessment of levees under extreme drought (ASCE 2015). Further investigations are required to quantitatively assess the impact of California's protracted drought on the short and long term behavior of levees, and also for timely action to strengthen and improve the resilience of California's levees to cope with drought. This chapter discusses, from a geotechnical engineering perspective, how the current California drought might threaten the integrity of levee systems. Catastrophic levee failures and major damages which occurred in similar drought situations are shown and discussed to illustrate the devastating impacts that the California drought might impose on existing levees. Several drought-induced, thermo-hydro-mechanical weakening processes are also discussed. While the focus of this chapter is more on levees throughout the Delta, the drought-induced weakening processes discussed herein also threaten levees in similar conditions in Northern California.

## Lessons from Previous Cases of Levee Performance in Drought

Anthropogenic modifications have been made to several sections along the Murray riverbanks in Australia to enhance their usability for farming and recreational purposes (Hubble and De Carli 2015); this type of work is analogous to levee construction. At the peak of the Millennium Drought (i.e., 2008-2009), cracking, strain softening, slumping, scouring, and eventually widespread mass failures occurred along sections of the riverbanks as a result of heavy rainfall. Hubble and De Carli (2015) stated that several of the observed cracks extended as much as 1.5 meters deep and 0.6 meters wide. The heavy rainfall events following the Millennium Drought also threatened the integrity of over 300 kilometers of levees throughout southeastern Australia (Todd 2010). Figure 2 depicts several of the failures which occurred along the Murray riverbanks after

the drought was superseded by heavy rainfall (Hubble and De Carli 2015). Figure 2a displays the circular slumping failures along the 150 meter section. The multi-beam bathymetry map in Figure 2b depicts the change in topography of the riverbanks after the failures. The smallest depths are indicated by red and the largest by dark blue, representing about 1 and 13 meter changes in topography of the riverbanks, respectively.

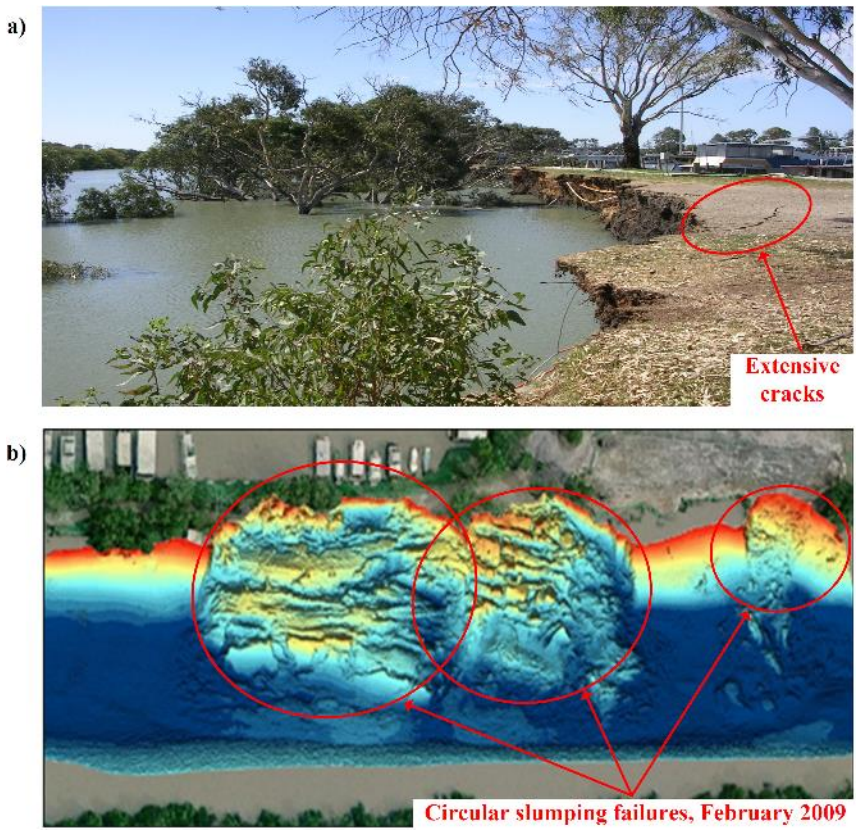


Figure 2 (a) Slumping riverbank failures during Millennium Drought and (b) Bathymetry map of failures

(figs. courtesy of Prof. Tom Hubble).

Another example of the impacts of extreme drought on earthen structures is the failure of the Wilnis Dike in the Netherlands (Van Baars 2005). The Wilnis Dike serves as a secondary dike, and the surficial soil layers in the vicinity of the Wilnis Dike failure

consisted mostly of a highly anisotropic deposit of peat overlying a thick layer of dense sand. During one of the driest summers in over 50 years, the Wilnis Dike failed in August 2003. Field inspections revealed small and large desiccation cracks in the peat material. Figure 3 shows the largest failure occurring in the Wilnis Dike. The failure consisted of a 10 meter horizontal translation that was triggered by the drought-induced cracks and other factors, namely, reduction in soil unit weight and shrinkage (Van Baars 2005). The horizontal translation of the dike led to rapid dissipation of water in the Wilnis Canal displacing approximately 2,000 residents in the Wilnis Village from their homes and placing roughly 600 houses under about half a meter of water (Van Baars 2004). Reduction in self-weight, shrinkage, and desiccation cracking of the peat material were identified to be the principal contributing factors to the failures of the Wilnis Dike during the unusually dry season in 2003 (Van Baars 2005).

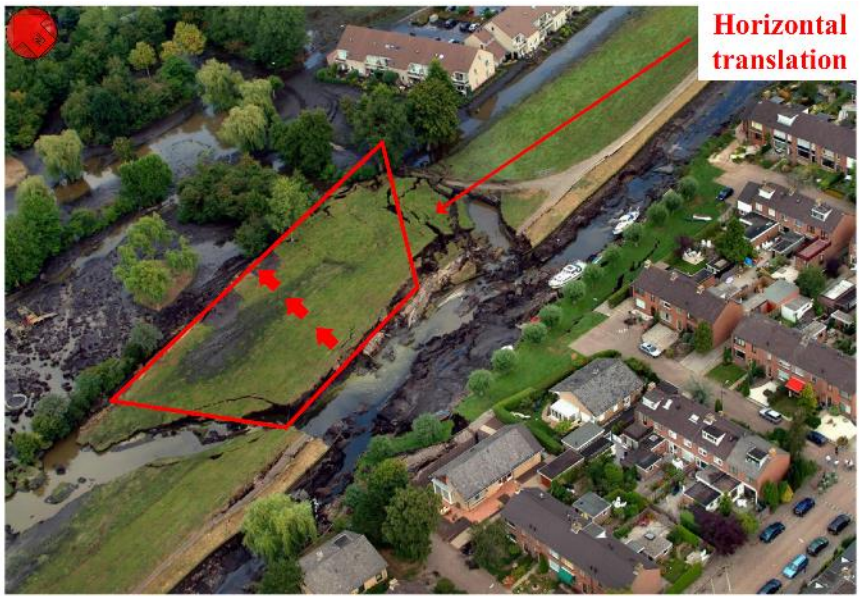


Figure 3 Horizontal Failure of Wilnis Levee, occurring in 2003 after a drought (image courtesy of Prof. Stefan Van Baars).

Additional studies have been conducted in the United States regarding the impact of drought stress on levees. In November 2004, the United States Army Engineer Research and Development Center conducted ponding tests on a section of the Retamal levee in the Lower Rio Grande Valley, Texas (Dunbar et al. 2007). The body and foundation of the Retamal levee is predominately comprised of high plasticity clay (Dunbar et al. 2007). The ultimate goal of the study was to delineate potential weakening and failure mechanisms in levees under extreme drought stress (Dunbar et al. 2007). Several areas along the Retamal levee showed signs of extensive surface cracks, soil drying, and internal erosion. It was noted that surface cracks extended into the core of the levee to a depth of about 2.7 meters (Dunbar et al. 2007).

**Status of California Levees**

In California, over 21,000 kilometers of urban and non-urban levees deliver two-thirds of drinking water, and protect dry land, homes, businesses, and agriculture in the Central Valley, Delta, and Northern California from flooding (CDWR 2011; LAO 2015). The levees throughout most of the Delta downstream of Sacramento are primarily non-urban levees which protect land that is at or below sea level and often continuously hold back water. On the contrary, the majority of levees throughout the Central Valley and Northern California are urban as they protect densely populated areas from flooding (CDWR 2011). The later levees are intermittently loaded and are designed to function only during flooding or high water levels. Drought-induced weakening mechanisms can also threaten the structural integrity of urban flood control levees throughout Sacramento, Stockton, and other cities in Northern California.

Resilience of California's levees, regardless of extreme drought, is a primary concern by considering the fact that the majority of California's levee systems are operating under rather poor reliability (LAO 2015). A high percentage of the levee systems in the Delta were constructed by settlers in the mid to late 18th century to protect agricultural lands from flooding. These levees are predominately comprised of poorly compacted, un-engineered mixtures of sandy, clayey, and organic soils. In addition, the vast majority of these marginal levee systems were built directly above deep layers of highly organic peaty soils (Reinert et al. 2014). It is noted that the original function for the Delta levees was to protect rich farmland that often flooded on a 2-5 year basis and not to restrict saltwater from intruding into the freshwater system. However, their role has changed with time and the Delta levees are currently critical for California in that agriculture and movement of water for the State Water Project and the federal Central Valley Project depend heavily on these levees (LAO 2015). This change in the Delta levees' role is primarily due to the major land subsidence experienced in the Delta. Failure of the Delta levees would inundate land that has subsided below sea level, drawing in seawater and consequently, contaminating the water supply.

Figure 4 illustrates the hazard ratings for urban (Figure 4a) and non–urban (Figure 4b) levees throughout the Sacramento and San Joaquin River Watersheds, reported by the California Department of Water Resources (CDWR 2011). The evaluation considered 478 and 2,386 kilometers of urban and non-urban levees, respectively. As can be seen, 51 and 55% of urban and non-urban levees evaluated, respectively, were classified as high hazard, indicating that they are in danger of failing during an earthquake or flood event. It is important to note that these classifications were performed before the ongoing extreme

drought commenced. Assuming the drought will further degrade the levees integrity, the functionality of the aging levees will continue to decrease unless strategic actions are taken to implement some level of maintenance and rehabilitation approaches (NRC 2012).

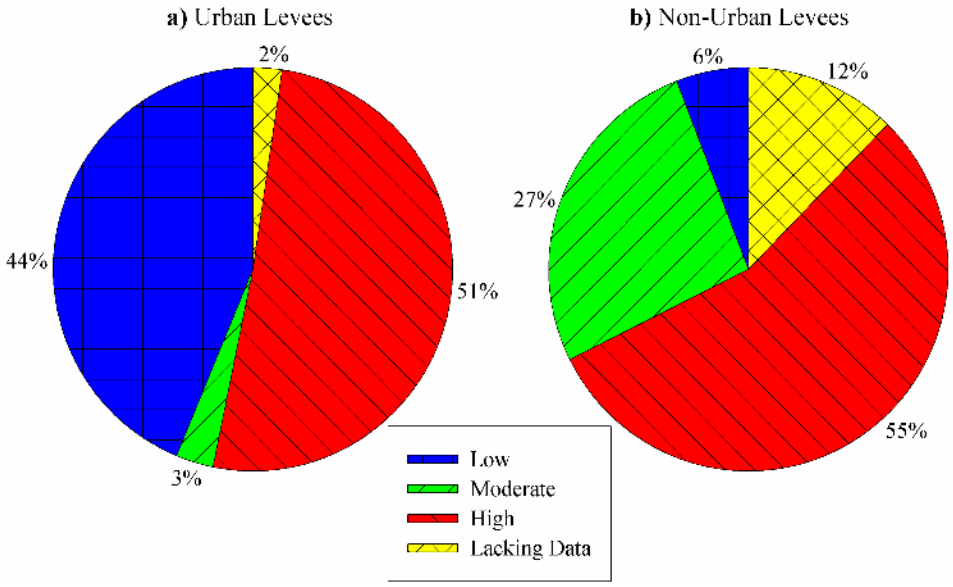


Figure 4 Hazard classifications of (a) urban and (b) non-urban levees in California (data from CDWR 2011).

A risk analysis was conducted in 2006 to compare consequences of California levee failure before and after drought (Vicuña et al. 2006). The analysis indicated that levee failure in the post-drought scenario resulted in land fallowing of approximately 1 million acres in the San Joaquin Valley, in addition to a farm productivity loss of roughly $250 million. Levee failure in the before-drought scenario was estimated to result in land fallowing of approximately 700,000 acres and a decline in farm profits of about $100

million (Vicuña et al. 2006). These figures and economic impacts are anticipated to rise given the inflation and worsened drought conditions.

## Potential Weakening Mechanisms in Levees Due to Drought Stress

In order to properly investigate adverse impacts of the ongoing drought on the structural integrity of California's levees, it is necessary to quantify the effects of drought on stabilizing and destabilizing factors contributing to the stability of levees. As schematically shown in Figure 5, several drought-induced weakening mechanisms can adversely impact the integrity of earthen structures such as levees. The mechanisms include, but are not limited to, soil strength reduction, desiccation cracking, land subsidence and erosion, fissuring and soil softening, and soil organic carbon (SOC) oxidation (e.g., Dunbar et al. 2007; Vicuña et al. 2006; Port and Hoover 2011; Brooks et al. 2012; Vardon 2014; ASCE 2015; Vahedifard et al. 2015a). These potential drought-induced weakening mechanisms and their threats on levee stability are discussed in the subsequent sections.

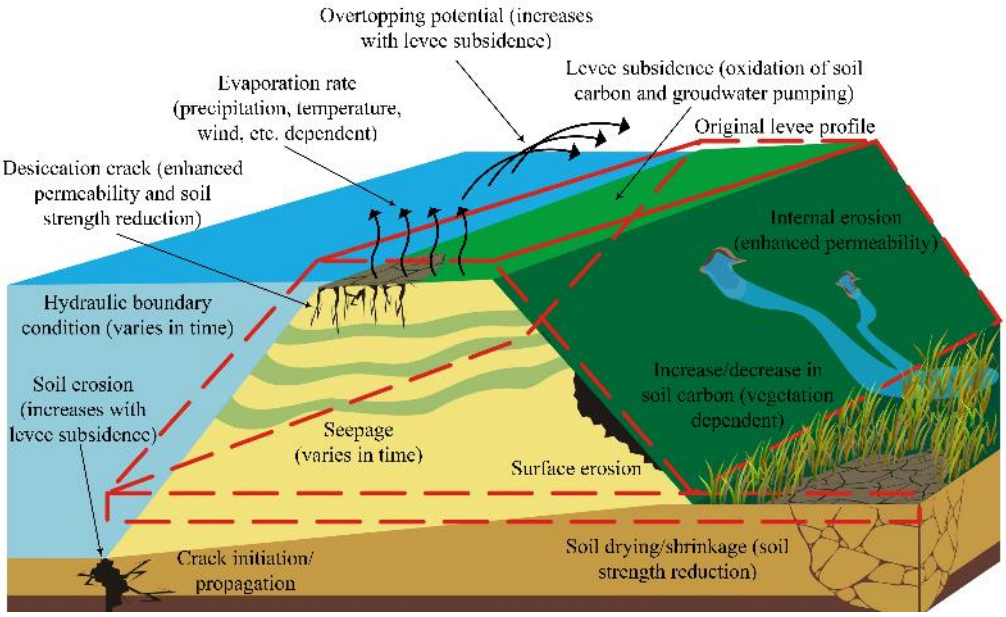


Figure 5 Potential weakening mechanisms imposed on earthen levees from drought.

**Influence on Soil Shear and Tensile Strength**

Soil strength is the primary stabilizing factor maintaining the structural reliability of any earthen structure including earthen levees. The imposition of drought-induced weakening mechanisms such as desiccation cracks in earthen levees can lead to instabilities by reducing soil strength. The shear strength and tensile strength of soils are an indication of a soil's capability to resist external compressive and tensile stresses, respectively, without failing (e.g., Lu and Likos 2006; Lu et al. 2009). Most of the soils used in the structure of a levee are under an unsaturated condition above the phreatic surface. Shear and tensile strengths are not constant for soils under variably saturated conditions and therefore, these two strength properties are highly dependent on soil saturation and matric suction (or negative pore water pressure) (e.g., Vahedifard et al. 2015c). Likewise, under various degrees of saturation and matric suctions, the magnitude

and variation of shear and tensile strengths can have profound impacts on the stability of earthen levees.

The shear and tensile strength of variably saturated soils can be captured using the suction stress (e.g., Lu and Likos 2006). Lu and Likos (2006) presented a unified formulation capturing changes in the effective stress under both saturated and unsaturated conditions as:

$$\sigma' = \sigma - u_a - \sigma^s \quad (1)$$

where $\sigma'$ represents the effective stress, $\sigma$ represents the total stress, $u_a$ is the pore air pressure, and $\sigma^s$ defines the suction stress. The effective stress can be conceptualized as the force that keeps an assemblage of particles rigid. Suction stress is used to quantify the impacts of soil suction and variations in saturation on the effective stress. Lu et al. (2010) extended Bishop's (1959) effective stress model to represent changes in the effective stress due to varying matric suction and soil saturation as follows:

$$\sigma^s = -S_e(u_a - u_w) \quad (2)$$

where $(u_a - u_w)$ represents the matric suction, and $S_e$ represents the effective degree of saturation (or normalized water content). The effective degree of saturation is used to capture the contribution of suction stress in an unsaturated soil matrix due to the coupled effects of matric suction and surface tension (Lu et al. 2010). Using van Genuchten (1980) - Mualem's (1976) model, $S_e$ can be expressed as a function of matric suction by employing a two parameter equation in the following form (Lu et al. 2010):

$$S_e = \left\{\frac{1}{1+[\alpha(u_a - u_w)]^n}\right\}^{\frac{n-1}{n}} \quad (3)$$

where $\alpha$ and $n$ are fitting parameters delineating the relationship between matric suction and soil saturation. As defined, $\alpha$ approximates the inverse of the air-entry pressure and $n$ is a measure of the distribution of the soil's pore size. The air-entry pressure represents the point at which air is pushed out of a soil's pore space (i.e., the system approaches saturation). In general, fined-grained soils, in comparison to coarse-grained soils, support larger air-entry pressures and consequently, higher matric suctions (Lu et al. 2010).

The unified effective stress presented in Eq. 1 can be used to define the shear strength ($\tau$) of variably saturated soils as:

$$\tau = c' + [(\sigma - u_a) - \sigma^s]\tan\phi' \quad (4)$$

where $c'$ is the effective cohesion intercept which is theoretically zero for coarse-grained soils and greater than zero for fine-grained soils, the difference $(\sigma - u_a)$ delineates the net normal stress, and $\phi'$ is the effective friction angle. Generally, coarse-grained soils exhibit greater values of $\phi'$.

Employing the suction stress concept, Lu et al. (2009) defined the isotropic uniaxial tensile strength of variably saturated soils as follows:

$$\sigma_t = 2\tan\phi'_t \tan\left(\frac{\pi}{4} - \frac{\phi'_t}{2}\right)\sigma^s \quad (5)$$

where $\sigma_t$ represents the tensile strength and $\phi'_t$ is the true angle of friction under a nonlinear Mohr-Coulomb failure envelope.

Figure 6 illustrate the influence of the effective degree of saturation on the magnitude and variation in shear strength and suction stress. Input values for the soil shear strength parameters (i.e., $c'$ and $\phi'$) were selected based on values reported by

Reinert et al. (2014) for a California levee sand. Furthermore, the selected input values for $n$, $\alpha$, $\phi'_t$, and soil unit weight ($\gamma$) were the same as those used by Lu et al. (2009) for three fine sands with different particle-size distributions. In Figure 6a, z = 9 m represents the depth at which the total stress was calculated. Moreover, 9 m is a typical height for the body of an earthen levee. As demonstrated in Figure 6, if the soil is too wet (e.g., extreme rainfall events), or inversely, too dry (e.g., drought) the air-water interface areas in soil will diminish, resulting in infinitesimal to zero suction stress, and smaller shear stress than those between $0\% < S_e < 100\%$. Such changes in suction stress and shear strength can significantly impact the stability of earthen slopes (e.g., Vahedifard et al. 2015b).

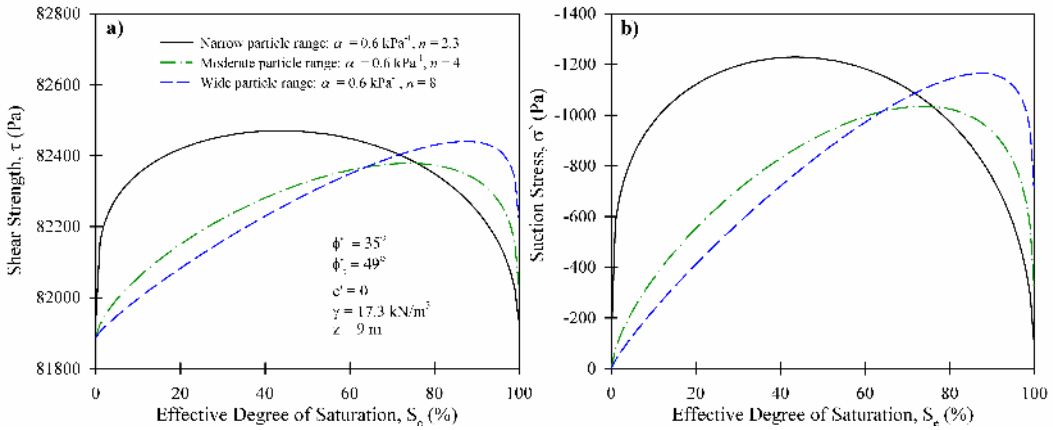


Figure 6 (a) Shear strength and (b) Suction stress characteristic curves (SSCCs).

Figure 7 displays the relationship between the tensile strength characteristic curve and the soil water characteristic curve with various effective degrees of saturation. As shown, the tensile strength of sand exhibits a non-monotonic trend with variations in $S_e$.

Too dry or too wet conditions will lead to reductions in the tensile strength. Also, an increase suction might increase tensile strength of the intact soil, but it also causes cracks that can limit the mass strength.

As it can be seen in Figure 7, sands with a smaller pore size distribution sustain greater inter-particle isotropic tensile stress and matric suction, resulting in larger tensile strength. However, between $0\% \leq S_e \leq 20\%$, sands with a wide particle-size range and pore size distribution can undergo larger reductions in tensile strength. This degradation in the tensile strength reinforces the need for its consideration under extreme drought conditions.

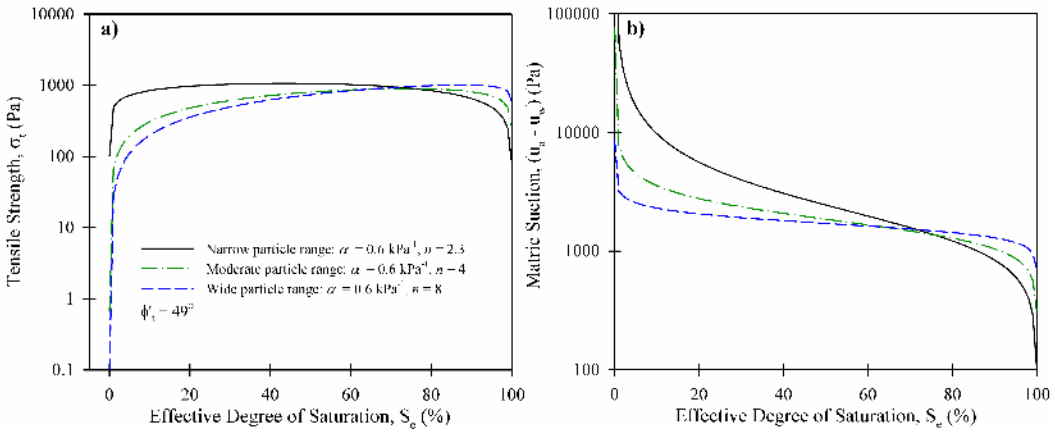


Figure 7 (a) Tensile strength characteristic curve and (b) Soil water characteristic curve.

**Desiccation Cracking and Soil Softening**

Extreme drought can further adversely impact the stability of earthen levees by softening the soil and inducing desiccation cracks in their body and foundation (e.g., Dunbar et al. 2007; ASCE 2015). Some levees throughout California, such as those in the

Delta, continuously hold water behind them. The depths of desiccation cracks in these levees are presumably limited by the position of the phreatic surface within the levee. As opposed to Delta's levees, urban levees in the Central Valley and Northern California are intermittently loaded. Drought-induced desiccation cracking can be of greater consequence for the integrity of these intermittently loaded levees that may become completely dry during drought. It is important to note that desiccation cracks are also a problem during periods of heavy precipitation because they permit infiltration to considerable depths before the cracks can be closed by re-absorption of water

It is noted that many of the levees throughout the Delta are predominately comprised of sandy, clayey, and peaty soils. Sandy and peaty soils contain a significant amount of large pores and may be more sensitive to water loss during an extreme drought event. Conversely, clayey soils have very few macro-pores and therefore, are more likely to retain water. However, clayey soils (i.e., fine-grained soils) are extremely susceptible to desiccation cracking. Desiccation cracking behavior is governed by a large number of factors, namely, mineral composition, temperature, relative humidity, layer thickness and layer size (e.g., Péron 2009; Tang et al. 2011). Several studies (e.g., Skempton et al. 1969; Van Baars 2005; and Dyer et al. 2009) have investigated the adverse effects of clay desiccation fissuring and softening on earthen structures. Fissures refer to narrow openings or cracks whose dimensions are largely governed by soil moisture, plasticity, and temperature (Dyer et al. 2009). Tang et al. (2011) noted that an overall increase in temperature and prolonged periods of no precipitation (i.e., drought) can lead to long-term soil drying, which eventually leads to shrinkage and corresponding desiccation cracking. Hudacsek et al. (2009) used centrifuge tests to show how soil softening and

irreversible creep due to pore-pressure cycling induced swelling and shrinking in clayey soils, causing desiccation cracking and eventually leading to serviceability failure in earthen structures. Such behavior in the fine-grained soils of levees can lead to more significant structural instabilities such as slides, flows, or falls (Tang et al. 2011). For example, a material with a dry density below its average dry density may increase the risk of sliding in earthen levees (Vardon 2014).

In the case of desiccation cracking, prolonged rainfall events during drought have been shown to influence partially saturated soil zones by up to 12 meters below the ground surface (Baram et al. 2012). Desiccation cracks expose the soil to rapid infiltration leading to large increases in pore pressures at uncharacteristic depths (Tang et al. 2011). Large increases in pore pressures, in addition to water infiltrating into open cracks, can lead to significant decreases in the effective stress (Eq. 1), which can drive an earthen structure to go past its limit state (Factor of Safety, FS < 1) and increase the risk of failure. It is important to note that limit state may not necessarily denote instability in the form of immediate catastrophic failure. Continual motion causing a reduction in soil shear strength can lead to catastrophic failure. For instance, the 1963 Vaiont dam failure in Northern Italy occurred after a prolonged period of creep leading to strain softening. In time, the small increases in load led to disproportional increases in velocity (i.e., creep) and the driving force (i.e., weight of the structure) increased due to losses in shear resistance along the failure surface.

**Land Erosion and Subsidence**

Drought-induced land subsidence and erosion can threaten the integrity of levee systems in California by reducing lateral support and shear resistance, making the

systems more susceptible to structural instabilities (Mount and Twiss 2005). Levees in the San Joaquin Delta are founded on thick layers of peat and the unique macro-structure of peat poses a critical challenge in evaluating subsidence (Reinert 2014; Cappa et al. 2015). Progressive land subsidence can directly threaten levee structures by exacerbating the risks of water rising over the tops of levees (referred to as overtopping). For example, the catastrophic levee failures occurring in August 2005 in New Orleans, Louisiana during the peak storm surge of Hurricane Katrina were attributed to a rapid subsidence period taking place from 2002 – 2005. Dixon et al. (2006) stated that the height of the subsided levees was not great enough to sustain the storm surge, hence commencing the failures, which resulted in more than 1,300 deaths and over $100 billion worth of economic loss (Briaud et al. 2008).

Land erosion can provide potential pathways for cracking, leading to enhanced permeability and reduction in the stability of an earthen slope (Vardon 2014). Cutting off the land from flood waters in the San Joaquin Delta has barred replacement of sediments. This has led to dramatic land subsidence and erosion as previously flooded, low-oxygen soils have been drained and aerated, losing significant amounts of organic carbon in the process (Mount and Twiss 2005; Deverel and Leighton 2010). Certain parts of the central and western San Joaquin Delta currently sit more than 3 meters below sea level (Lund et al. 2007). Sea level rise is projected to be a consequence of climate change, leading to an increased risk of coastal flooding. Together, land subsidence and rising sea levels have rendered the region behind the levees increasingly vulnerable to flooding (Zhu et al. 2007), with particular susceptibility noted for the western and central San Joaquin Delta (Lund et al. 2007).

Land subsidence, and subsequent erosion, further increases when groundwater is being consumed at a rate faster than it is being replenished by groundwater recharge. Significant land subsidence due to excessive groundwater pumping has been recorded in the Delta over the past few years. Brooks et al. (2012) used Interferometric Synthetic Aperture Radar (InSAR) measurements to project future land subsidence and potential levee overtopping. They predicted that, along with the current global estimated sea-level rise, there will be small isolated regions in the San Joaquin Delta that will subside by approximately 0.5 meters by the year 2025. By 2050, their predictions showed estimates of widespread subsidence of more than 0.5 meters. Brookes et al. (2012) predicted that all San Joaquin Delta levees will have subsided below the 0.5 meter threshold by the year 2100, which could eventually lead to potential levee overtopping ensued by very high risk flooding throughout the Delta. Recent results from a long-term remote sensing-based monitoring study showed that land subsidence in parts of the Delta has reached historical rates of around 5 centimeters per month (Farr et al. 2015), several times larger than pre-drought subsidence rates (i.e., as much as 3.4 cm per year) estimated for the same area (Deverel and Leighton 2010; Brookes et al. 2012). Figure 8 below displays the total subsidence occurring in the Delta for the period May 2014 to January 2015 (Farr et al. 2015). The aforementioned subsidence rates of 5 centimeters are clearly visible around El Nido and Corcoran.

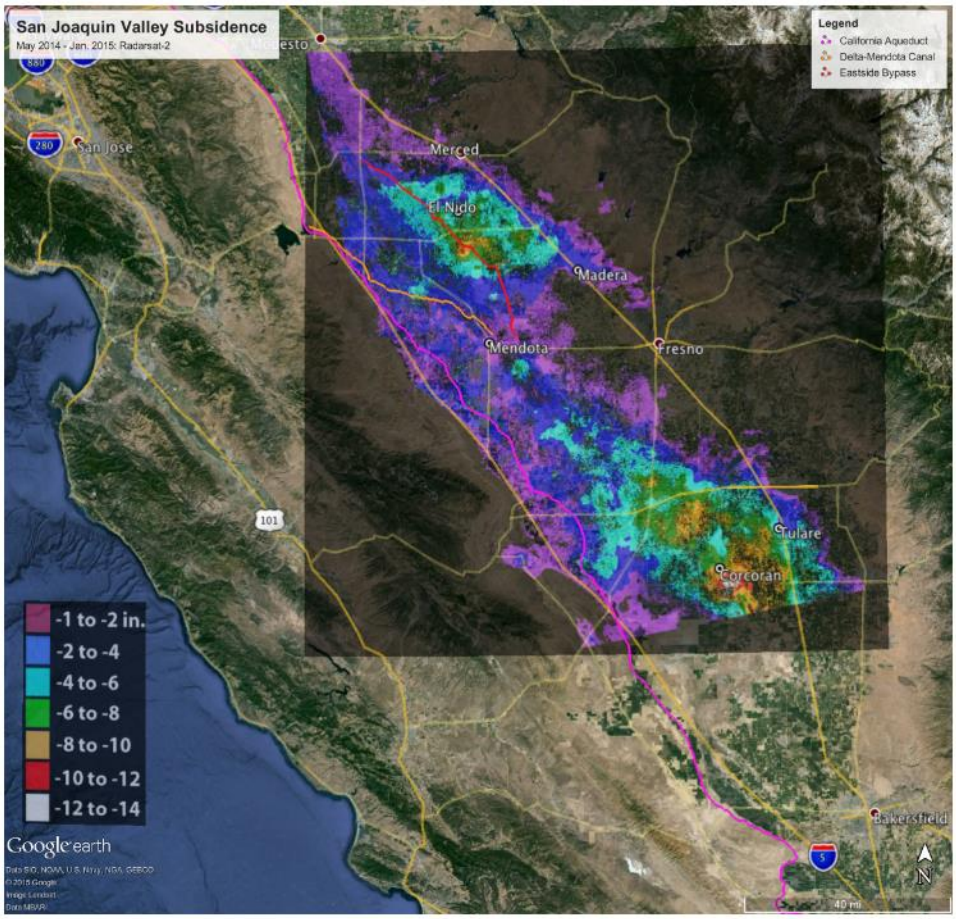


Figure 8 Total land subsidence occurring in the Sacramento-San Joaquin Delta (after Farr et al. 2015).

**Resilience of California Levees under a Multi-Hazard Scenario**

While the focus of this article is about the effects of drought, it is prudent to consider a multi-hazard scenario when assessing the performance of California's levees during drought. It is almost inevitable that drought is superimposed or followed by other climatic conditions such as severe flooding, storm surges, high temperatures, sea level rise, and extreme rainfall events, which can further threaten the structural integrity of levees. El Niño is also anticipated to hit California in 2016 with high temperatures, heavy rainfall, and storm surges, all resulting from changes in the distribution of warm water in

the Pacific Ocean (Prigg 2015). During the 1997 El Niño events, California experienced a 200% increase in rainfall as compared to preceding annual averages. These heavy rains (i.e., about 760 mm of rain in two months) prompted overtopping levee failures as well as avalanches throughout the Sacramento River Basin, displacing more than 120,000 individuals and resulting in approximately $35 million (1997 dollars) in economic loss (CERT.io 2015).

Additionally, the high seismicity level of California poses yet another challenge to the resilience of California's levees (e.g., Port and Hoover 2011; Reinert et al. 2014). There is a 67% chance that a 6.7 or greater magnitude earthquake will occur in the Delta Region in the next 20 years; an earthquake of this magnitude could induce over 140 levee failures as well as flood several islands instantaneously, leading to repair costs of more than $2.3 billion (Port and Hoover 2011).

In terms of flood hazard, the current warming trend will likely induce a 30 centimeters sea level rise in the next 25 years (Port and Hoover 2011). Such a threat is anticipated to increase the frequency of a 100-year peak tide to only a 10-year event, resulting in flooding of at least 27 islands in the Delta (Port and Hoover 2011). Sea level rise near the Delta's western end can also induce increases in seawater intrusion which could slowly disrupt water supply systems for several months to several years (Hank and Lund 2012).

CHAPTER III

# RAINFALL-TRIGGERED SLOPE INSTABILITIES UNDER A CHANGING CLIMATE: COMPARATIVE STUDY USING HISTORICAL AND PROJECTED PRECIPITATION EXTREMES

## Introduction

Landslides are natural hazards that often pose threats on both the societal and economical levels. In the United States, landslides are responsible for more than $1.6 billion in annual socioeconomic and environmental losses (e.g., Schuster and Highland 2001). They may be attributed to destabilizing factors such as soil desiccation and tensile cracking, land and surface erosion, soil fissuring and softening, and seismicity (e.g., Leshchinsky et al. 2015). However landslides are most frequently accredited to dynamic processes, namely, significant seasonal and long-term variations in rainfall; and under these type of extreme climatic conditions the aforementioned weakening mechanisms can accelerate landslide occurrences. Rainfall variations can have immense impacts on soil moisture and consequently, soil strength and the near-surface groundwater field. The groundwater field directly impedes the activation of deep-seated landslides. These types of landslides are classified as slopes failures which are a few meters in thickness and involve the movement of the surficial mantle and underlying bedrock (e.g., Coe and Godt 2012). In contrast, shallow landslides include translational slope failures that are a few meters thick, comprising of poorly consolidated soil mantle and underlying bedrock (e.g.,

Cascini et al. 2010; Lu et al. 2012). The frequency and magnitude of landslides are sensitive to extremes in the hydraulic cycle such as protracted drought, which increases groundwater extraction, hence, impeding groundwater recharge, leading to cessation of deep-seated landslides (e.g., Coe and Godt 2012). Shallow landslides, however, are typically triggered by meteo-climatic factors such as extreme rainfall events, rapid snowmelt, and antecedent rainfall (e.g., Sidle 2007; Melchiorre and Frattini 2012).

Landslide processes are typically assessed at local to regional scales (e.g., Coe and Godt 2012; Melchiorre and Frattini 2012). However, discerning these processes necessitates a comprehensive understanding of how they are affected by a changing climate (e.g., Farahmand and AghaKouchak 2013). Coe and Godt (2012) identified fourteen technical approaches to assess the impact of climate change on landslide activity. Coe and Godt (2012) categorized these approaches into three groups: 1) long-term monitoring of climate change and the corresponding response from landslides; 2) surveying approaches manifesting the association between climate change and landslides from historical data; and 3) future approaches that establish patterns between climate change and historical landslide activation. One shortcoming of the aforementioned approaches is that they are partially reliant on the so-called stationary assumption (i.e., statistics of extreme events will not vary significantly over a long period of time) (Coe and Godt 2012). However, climate change is anticipated to increase the frequency, intensity, and duration of climatic extremes in the future (e.g., Cheng and AghaKouchak 2014). There are two major issues that obstruct our advancement in fully understanding how landslide processes are affected by a changing climate including the high uncertainty in forecasting landslide activation due to heavy precipitation and improbability in

predicting precipitation and storm patterns (e.g., Coe and Godt 2012; Melchiorre and Frattini 2012). Moreover, landslide studies typically project mean precipitation data as it is very difficult to estimate the variations in the frequency and magnitude of extreme rainfall events (e.g., Coe and Godt 2012).

Among recent climate trends, extreme precipitation is recognized as one of the major causes for several instabilities in natural and engineered earthen structures (e.g., NRC 2008, 2013; Sorooshian et al. 2011). In fact, some areas (e.g., Northeast United States) throughout the United States experienced as much a 67% increase in heavy precipitation from 1958 to 2007 (USGCRP 2009). Similar trends have been reported throughout other parts of the world like the Korean Peninsula (e.g., KMA 2008), and such trends have prompted several rainfall-triggered instabilities in natural and engineered earthen structures (e.g., Leshchinsky et al. 2015). These cases highlight a crucial need for considering the increased intensity of extreme precipitation driven by climate change in the analysis, maintenance, and monitoring of existing infrastructure, as well as the design of future infrastructure (e.g., NRC 2008, 2013; Crozier 2010; ASCE 2015).

The performance of earthen structures against extreme precipitation is commonly analyzed using Intensity-Duration-Frequency (IDF) curves. These curves are established using historical rainfall data. Failing to recognize changes in statistics of extremes events (i.e., nonstationary condition) such as increased rainfall intensity when analyzing the performance of an earthen structure can lead to significant underestimations in the expected rainfall events that a structure may experience during its lifetime (e.g., Gregersen et al. 2013; Cheng et al. 2014; Vardon 2014). Thus, the impacts of future

(projected) precipitation patterns on the short and long term behavior of natural and engineered earthen slopes is an issue that deserves proper attention.

This study quantitatively investigates natural slope instabilities due to extreme precipitation events under climatic variations. Many of the weaknesses observed in previous studies (e.g., Coe and Godt 2012) lies in the input (e.g., historical precipitation patterns) and output data, rather than the methodology. To consider these weaknesses, as well as variations in the statistics of the future climate, the current study adopts a nonstationary approach, applied to climate model simulations, to analyze projected annual precipitation maxima. This approach would yield less uncertainty in the analysis of landslide modeling and improve our understanding of climate-induced changes in future extreme rainfall events (e.g., Cheng and AghaKouchak 2014; Cheng et al. 2014). Baseline and projected precipitation extremes correspond to an area near Seattle, Washington (WA). Both historical (baseline) and projected precipitation patterns are integrated into a series of fully coupled 2D transient unsaturated seepage finite element (FE) simulations. The responses of the baseline and projected FE models at a 7-day rainfall duration obtained for a 50-year recurrence interval are compared in terms of the factor of safety (FS), displacements, matric suctions (or negative pore-water pressure), degrees of saturation, and corresponding suction stresses.

## Intensity of Extreme Precipitation Events

Seattle, WA is selected as the study area for acquiring the historical and future IDF curves. The study area falls within the Northwestern quadrant of the U.S., which reportedly experienced a 16% increase in rainfall intensity from 1958 to 2007 (USGCRP 2009). This area is frequently susceptible to shallow and deep-seated landslides primarily

triggered by rainfall (e.g., Lu et al. 2012). A major rainfall-triggered landslide recently occurred in March 2014 about 100 kilometers north of Seattle in Snohomish County, WA. The landslide was characterized as a deep-seated slope failure. It has been reported that the spring of 2014 was the wettest on record in Seattle, which could have been a contributing factor towards the failure (e.g., Iverson et al. 2015). Approximately 48 centimeters of heavy rain had fallen at the Sea-Tac Airport in Seattle from February to March 2014. The Snohomish County landslide resulted in capital losses in excess of $50 million (Keaton et al. 2014).

To compare the effects of historical and future precipitation extremes on rainfall-triggered slope instabilities, this study uses two sets of IDF curves: baseline (historical) and projected (future). The baseline IDF curves are derived using a stationary framework, similar to the method outlined in Bonnin et al. (2006), which uses the National Oceanic and Atmospheric Administration (NOAA) Atlas 14 to obtain historical rainfall data. Current infrastructure design codes rely heavily on NOAA Atlas 14. The fundamental analysis outlined in Bonnin et al. (2006) is based on the Generalized Extreme Value (GEV) distribution assuming a stationary climate. This approach adopts ground-based observations of precipitation extremes (i.e., annual maxima) from the highest precipitation amount for various rainfall durations (e.g., 3- and 7-day). Furthermore, the standard GEV distribution is delineated as such (Coles 2001):

$$\Psi(x) = \exp\left\{-\left(1+\xi\left(\frac{x-\mu}{\sigma}\right)\right)^{-\frac{1}{\xi}}\right\}, 1+\xi\left(\frac{x-\mu}{\sigma}\right) > 0 \qquad (6)$$

The GEV distribution is described using the location ($\mu$), scale ($\sigma$) and shape ($\xi$) parameters. In a stationary approach, the statistical properties of the distribution are

independent of time, whereas the parameters [i.e., $\theta = (\mu, \sigma, \xi)$] under a nonstationary assumption are explicitly defined as a function of time.

In this study, the approach outlined in Cheng and AghaKouchak (2014) is adopted to derive projected nonstationary IDF curves. In this approach, $\mu$ is assumed to be time-dependent, while $\sigma$ and $\xi$ remain time invariant. Cheng and AghaKouchak (2014) used a linear time dependence whereby $\mu$ can be defined as follows:

$$\mu(t) = \mu_1 t + \mu_0 \tag{7}$$

Once the annual maxima are acquired from the highest precipitation amount (from historical rainfall data) for various rainfall durations, $\mu(t)$ is predicted based on the 95-th percentile of DE-MC sampled location parameters (i.e., $\tilde{\mu}$) over time (Cheng et al. 2014). For different exceedance probabilities ($p$), or recurrence intervals, the projected precipitation extremes can be defined as:

$$q_p = \left(\left(-\frac{1}{\ln p}\right)^{\xi} - 1\right)\frac{\sigma}{\xi} + \tilde{\mu}, (\xi \neq 0) \tag{8}$$

where $q_p$ represents the predicted future rainfall intensity.

The model parameters and uncertainty estimates for IDFs are estimated using a Bayesian approach available from the Nonstationary Extreme Value Analysis (NEVA) software developed after Cheng et al. (2014). The sampling approach used for estimating the parameters deduced by the Bayesian approach relies on the Differential Evolution Markov Chain (DE-MC). The DE-MC is a powerful tool for parameter estimation and has been widely used in the literature for generating large numbers of realizations from the posterior distributions of the model parameters (e.g., Ter Braak 2006; Vrugt et al.

2009; Cheng and AghaKouchak 2014). In this study, historical (1950-2009) and future (2040-2099) rainfall simulations available from the CMIP5 Representative Concentration Pathway (RCP) 8.5 are selected as inputs for deriving historical and future IDFs.

Future projections from 20 separate CMIP5 climate model simulations are used in a nonstationary model to derive future IDFs, where each single point represents an ensemble mean for given duration and return period. An ensemble includes a set of equally likely members from the climate model simulations. Based on Mann-Kendall trend test and Bayes factor statistics from NEVA (Cheng et al. 2014), a nonstationary model fits most ensemble members of future projections better than the commonly used stationary approach. In the nonstationary approach, GEV and the Mann-Kendall trend test are fitted separately to each ensemble member.

The current study considers a 7-day rainfall duration obtained for a 50-year recurrence interval for the Seattle region. Figure 9 presented below embodies the rainfall data implemented in this study. As can be seen, there is a significant difference between the baseline (Figure 9a) and projected (Figure 9b) rainfall intensities for each rainfall duration and respective recurrence interval. The relative change (Figure 9c) between the baseline and projected rainfall intensities increases with an increasing and decreasing rainfall duration and recurrence interval, respectively. For example, the projected 3-day rainfall intensity for the 50-year recurrence interval is only about 30% greater than the baseline intensity. On the other hand, the 7-day projected rainfall intensity for the same recurrence interval is approximately 87% higher than that obtained under the stationary approach. Furthermore, the relative difference between the baseline and projected rainfall intensities for the 3- and 7-day rainfall durations increases to 39% and 104%, for the 2-yr

recurrence interval. Further information regarding the nonstationary framework implemented in this study can be found in Cheng and AghaKouchak (2014).

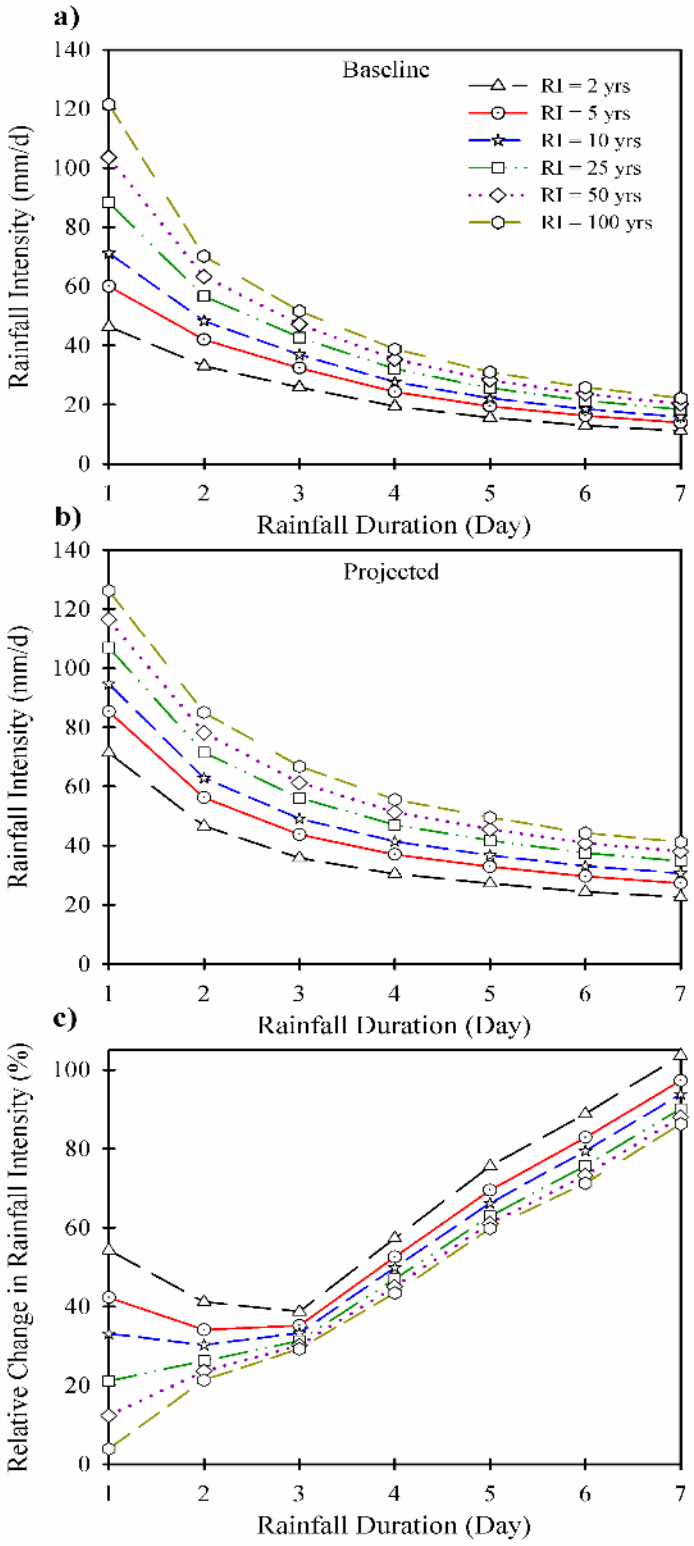


Figure 9 (a) Baseline and (b) Projected intensity duration frequency estimates, and (c) Relative percent change in rainfall for Seattle using GEV distribution.

**Fully Coupled Numerical Modeling of Transient Unsaturated Seepage**

A fully coupled FE analysis is executed to capture the behavior of a natural earthen slope under transient unsaturated seepage conditions. The analysis is simulated using the 2D FE commercial code RocScience RS$^2$. Biot's fully coupled pore pressure-stress equation is implemented in RS$^2$ to capture the nonlinear behavior of the porous elastic soil medium, where the fluid-solid coupling is accomplished through conditions of compressibility and continuity (e.g., Smith and Griffiths 1997) as shown in the following governing equation:

$$\frac{K\prime}{\gamma_w}\left[k_x\frac{\partial^2 u_w}{\partial x^2}+k_y\frac{\partial^2 u_w}{\partial y^2}+k_z\frac{\partial^2 u_w}{\partial z^2}\right]=\frac{\partial u_w}{\partial t}-\frac{\partial p}{\partial t} \quad (9)$$

where $K\prime$ demarcates the bulk modulus of the soil; $\gamma_w$ represents the unit weight of water; $u_w$ is the pore-water pressure; and $p$ is the mean total stress. To obtain equilibrium in 2D space, and in the absence of body forces, the gradients of the pore-water pressure in Biot's equation are used to augment the corresponding gradients of effective stress (e.g., Smith and Griffiths 1997). Moreover, Biot's governing equation is analyzed for equilibrium in RS$^2$ for each respective time increment under transient unsaturated seepage induced by the imposed baseline and projected surface infiltration boundary conditions.

**Numerical Modeling and Input Parameters**

A homogenous silty soil slope (Figure 10) is used to illustrate the impact of the baseline and projected precipitation extremes on the response of a natural slope. The model includes a 15-m high slope with 56 degree inclination. Similar slope geometries are reported in the literature for landslide modeling in the Seattle area (e.g., Lu et al.

2012). The analysis implements the classic effective shear strength parameters (i.e., c′ and ϕ′) along with van Genuchten (1980)-Mualem (1976)'s soil-water characteristic curve (SWCC) and hydraulic conductivity function (HCF). The SWCC and HCF fitting parameters $n$ and $\alpha$ used in this study are adopted after Lu et al. (2012). The fitting parameter $n$ is a measure of the soil's pore-size distribution while $\alpha$ approximates the air-entry pressure. The HCF, along with $n$ and $\alpha$, are directly implemented into RS$^2$ by adding *hydraulic* material properties to the silty soil. The SWCC and HCF for the silty soil used in the FE effective stress analysis are displayed in Figure 11. In addition, the soil properties are presented in Table 1.

As displayed in Figure 10, a FE mesh consisting of 1,469 eight-node quadrilateral elements is employed to discretize the soil material. The density of the elements is refined within approximately 2 meters below the surface infiltration boundary of the slope to capture the higher expected displacements and plastic behavior in the soil from the imposed rainfall intensities.

As can be seen in Figure 10, the left and right sides of the domain are pinned, enabling movement in the vertical direction while restricting movement in the horizontal direction. Additionally, the bottom boundary of the domain is fixed, restricting movement in both the x- and y-directions. For hydraulic boundary conditions, the baseline and projected rainfall intensities (Figure 9) are imposed along the surface infiltration boundary of the slope.

The simulation for each model (i.e., stationary versus nonstationary) consists of three stages: stage 1: steady-state seepage using annual rain to generate initial conditions (t = 0); stage 2: transient seepage using the corresponding 7-day precipitation extreme (t

= 1 day to t = 7 days); and stage 3: 8 days of transient seepage using annual rain to monitor the post-extreme rainfall performance of the slope (t = 8 days to t = 15 days). It is noted the stage 3 simulation was continued until t = 40 days but no meaningful change was observed in pore-water pressures after t = 15 days. Initial conditions are achieved through a steady-state seepage analysis by imposing the infiltration boundary with baseline and projected rainfall intensities of 2.9 and 3.1 mm/d, separately. These rainfall intensities used to generate the initial conditions represent annual precipitation amounts for the study area. After the initial conditions are achieved in each model, a transient seepage analysis is conducted by imposing 7-day baseline and projected rainfall intensities of 20.2 and 38.0 mm/d, respectively, along the slope boundary. A seepage face condition is employed for the simulated rainfall intensities. Such condition permits runoff when the rainfall intensity exceeds the infiltration capacity of the soil. The location of the water table is fixed horizontally at 2 meters below the toe of the slope while the left, right, and bottom segments of the domain are considered to be no-flow boundaries.

Slope stability FE models calculate FS as the ratio of the average shear strength of the soil and the average shear stress exhibited along some critical slip plane. Typically a FS of approximately 1.5 is recommended in the analysis of natural and engineered earthen slopes. Based on the aforementioned definition for FS, the current study employs the shear strength reduction (SSR) method in $RS^2$ to determine the strength reduction factor (SRF) that brings the model slope to its limit state (FS = 1). This is done by gradually increasing the reduced effective shear strength parameters until the slope reaches the verge of failure. When the slope has approached its limit state, the SRF is equal to the FS of the slope.

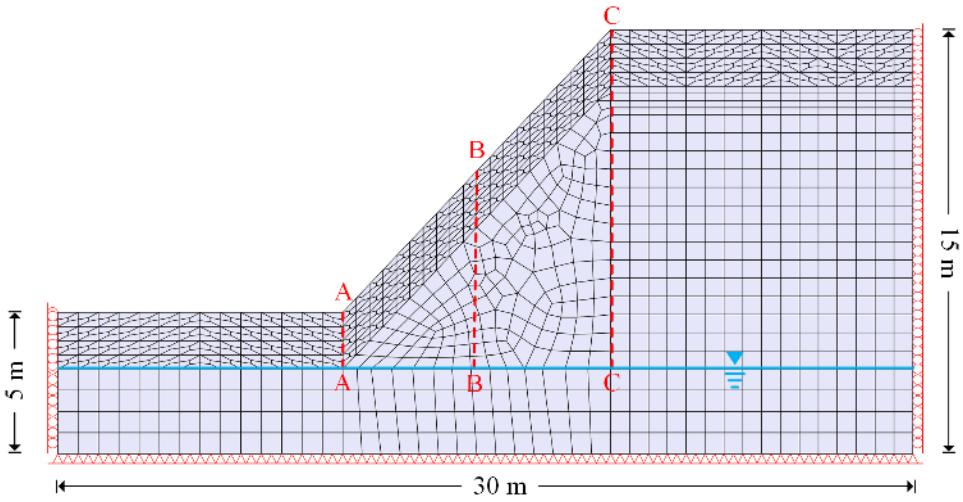


Figure 10 Finite Element (FE) mesh used in transient unsaturated seepage analysis.

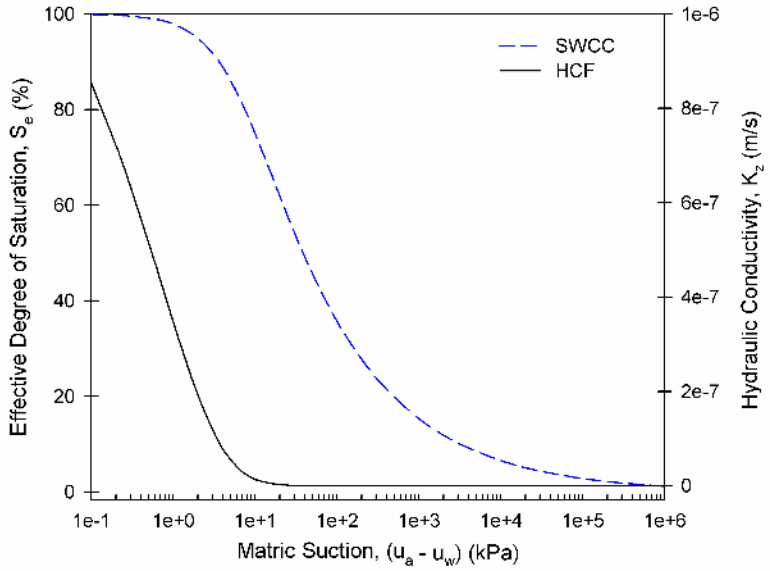


Figure 11 Soil-water characteristic curve (SWCC) and Hydraulic Conductivity Function (HCF) for silty soil

(after Lu et al. 2012).

Table 1 Material and hydraulic properties of silty sand used in FE analysis

| Parameter | Symbol | Unit | Value |
|---|---|---|---|
| Unit weight | $\gamma$ | $kN/m^3$ | 20 |
| Young's Modulus | E | kPa | 10000 |
| Poisson's Ratio | $\nu$ | - | 0.33 |
| Porosity | $\eta$ | - | 0.396 |
| Cohesion | $c'$ | kPa | 10 |
| Angle of friction | $\phi'$ | degrees | 30 |
| Saturated volumetric water content | $\theta_s$ | - | 0.46 |
| Residual volumetric water content | $\theta_r$ | - | 0.034 |
| Saturated hydraulic conductivity | $K_s$ | m/s | 3.39E-08 |
| Fitting parameter related to pore-size distribution | n | - | 1.37 |
| Fitting parameter related to air-entry pressure | $\alpha$ | 1/m | 1.6 |

## Results and Discussions

The variances between the commonly used historical and projected 7-day extreme precipitations are evaluated here by associating their effect on the stability of a natural earthen slope. While the 7 day rain intensity is applied to each model, the slope performance is monitored daily from t = 1 to t = 7 days. The impacts of the two precipitation extremes are compared in terms of the displacements, pore-water pressures, degrees of saturation, suction stresses, and FS.

The results displayed in Figure 12 are representative of the simulated baseline and projected relative displacements (Figures 12a-12c), degrees of saturation (Figures 12d-12f), and pore water pressures (Figures 12g-12i) under the transient unsaturated seepage conditions. As demonstrated in Figure 10, the results are plotted along three cross

sections of A-A (toe), B-B (middle), and C-C (crest). It is noted that displacements for each cross-section are plotted relative to that under the initial condition (i.e., t = 0). As can be seen, the imposed baseline rainfall intensity underestimates the displacement, saturation, and pore-water pressure in the model slope over the entire rainfall duration. Under the initial conditions in Figure 12, the small variations in performance along the three cross-sections are a manifestation of the minute difference between the imposed annual baseline and projected rainfall intensities (i.e., approximately 7.3% difference). As shown in the cross-section A-A, the toe exhibits the smallest displacement due to the resistance offered at this section. Once the annual rain is superimposed by a 7-day extreme event, the difference between the displacement, saturation, and pore-water pressure under the simulated baseline and projected rain intensities becomes more apparent.

In Figure 12, the greatest change between the performance metrics under the baseline and projected precipitation extremes can be seen in the upper slope (i.e., cross-section C-C). The projected rainfall intensity in the upper slope prompts a sliding that is approximately 95% greater than that under the baseline conditions at t = 1 day, for z = 0. It can be seen that the projected rain degrades slope performance as much as 2 days before the baseline rain. For example, the displacements, saturations, and pore-water pressures along cross-sections B-B and C-C are nearly identical under the baseline and projected rains, for t = 5 and 3 days, respectively. Such variations are attributed to the 87% increase in rain intensity from the stationary to the nonstationary condition.

While the 7-day rain persists in Figure 12, there can still be seen an apparent difference between the baseline and projected displacements, saturations, and pore-water

pressures. For example, the slope performance under the projected rainfall at t = 5 days is less than that under the baseline rain at t = 7 days. In fact, the pore-water pressure along the center of the slope (i.e., cross-section C-C) under the projected rainfall increases above 0 at t = 5 days, whereas the pore-water pressure remains negative for t = 7 days under the baseline rain. This indicates that the suction is diminished and so, is no longer contributing to the stability of the slope under the projected rain intensity beyond t = 5 days. Such behavior can significantly reduce the shear strength of the soil, leading to an increased risk of slope failure.

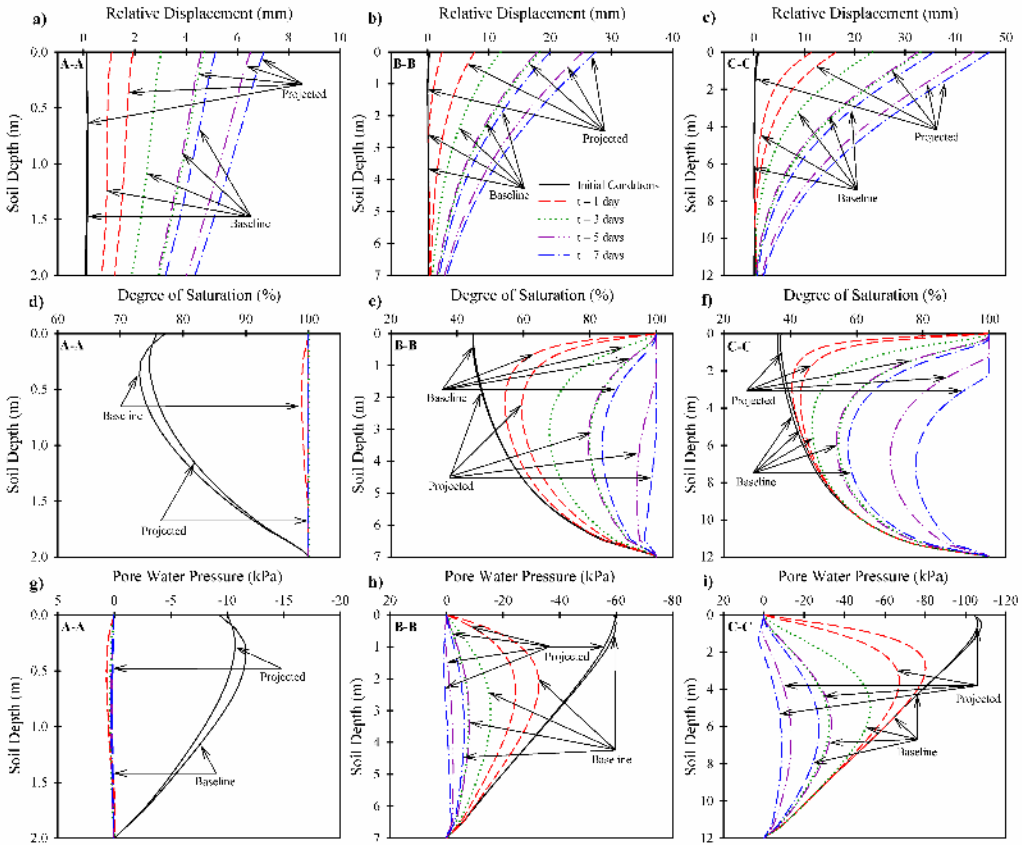


Figure 12 Simulated relative displacement, degree of saturation, and pore water pressure between baseline and projected rainfall.

Effective degree of saturation, $S_e$, and suction stress, $\sigma^s$, are two other parameters of interest that affect the strength of unsaturated soils (Robinson and Vahedifard 2015; Vahedifard et al. 2015d). Soil strength is the primary factor contributing to the structural stability of any earthen structure such as a natural slope (e.g., Fredlund and Rahardjo 1993; Vanapalli et al. 1996; Vahedifard et al. 2015a). The interactive thermodynamic free energy collectively represented by the suction stress in unsaturated soils can exist in the form of van der Waals forces, electric double-layer forces, surface tension, and soil-fluid air-interface forces resulting from matric suction (e.g., Lu et al. 2010). The current study employs the following equation for $\sigma^s$ proposed by Lu et al. (2010):

$$\sigma^s = -S_e(u_a - u_w) \tag{10}$$

The closed-form solution for $\sigma^s$ is an extension of Bishop's (1959) effective stress representation. Lu et al. (2010) verified the suction stress equation using experimental data obtained from 20 different soil types found in the literature. In addition, the suction stress-based effective stress representation has been successfully used to assess active earth pressures (e.g., Vahedifard et al. 2015b), slope stability (e.g., Griffiths and Lu 2005; Vahedifard et al. 2015c), and bearing capacity (e.g., Vahedifard and Robinson 2015) in unsaturated soils. The effective degree of saturation is defined as follows:

$$S_e = \frac{S - S_r}{1 - S_r} \tag{11}$$

where $S$ represents the pore-water saturation and $S_r$ is the residual saturation.

Figure 13 below compares the impacts of the baseline and projected precipitation extremes on the simulated $S_e$ with time, for three different depths along each cross-section. Figures 13a through 13c show the simulated $S_e$ over a 7-day rainfall duration,

whereas Figure 13d through 13f demonstrate the relative percent change in $S_e$ between the stationary and the nonstationary condition. A positive change is symbolic of an increase in $S_e$ from the stationary to the nonstationary condition, whereas a negative change indicates a decrease in $S_e$. Figure 13a shows that the wetting front progresses beyond the toe of the slope at just 3 days after the heavy rain commences (i.e., $S_e$ = 100%). As can be seen, the upper slope (i.e., cross-section C-C) exhibits the greatest change in $S_e$ under the stationary and the nonstationary condition between t = 1 day and 3 days. This sudden change is a result of the difference in the pore pressure increase between the baseline and projected rain intensities. For example, a 40 kPa increase in the pore pressure from t = 1 day to 3 days, at z = 5 m, under the projected rain prompts a 20% increase in $S_e$. In contrast, the pore pressure at the same depth and for the same time interval under the baseline rain only increases approximately 20 kPa, and thus only increases $S_e$ by about 5%.

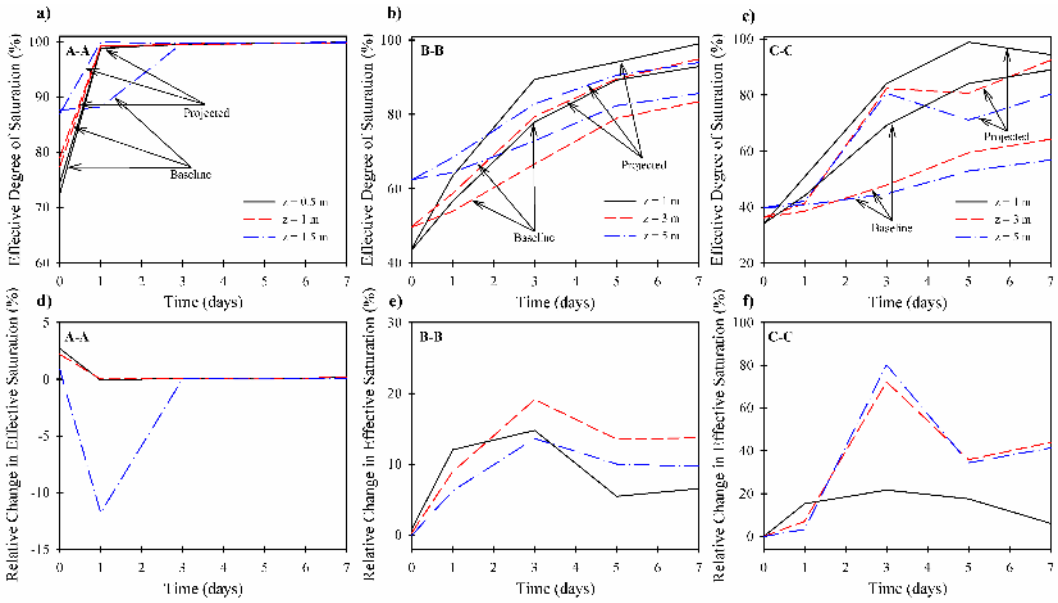


Figure 13 Simulated effective degree of saturation ($S_e$) and relative percent change between baseline and projected precipitation extremes.

Figure 14 shows the difference in the simulated suction stress over time between the baseline and projected precipitation extremes, for three depths along each cross-section. The figure shows that $\sigma^s$ in each cross-section, for t = 0, does not vary meaningfully between each of the imposed rainfall intensities. It is attributed to the small difference between the baseline and projected annual precipitation extremes. However, the difference in $\sigma^s$ between the baseline and projected rainfall intensities becomes more evident once the 7-day heavy rain begins (see Figures 14d – 14f). The upper and middle slope boundaries show similar trends in the relative percent change in $\sigma^s$. In detail, the upper slope at t = 1 day displays a $\sigma^s$ under the nonstationary condition that is approximately 20, 10, and 5% greater than that under stationary conditions, for z = 1, 3, and 5 m, respectively. For the same section, the relative percent change in $\sigma^s$ at z = 1 m

increases to a maximum of about 85% up to t = 5 days, while the relative percent change in $\sigma^s$, for z = 3 and 5 m, is greatest at t = 7 days.

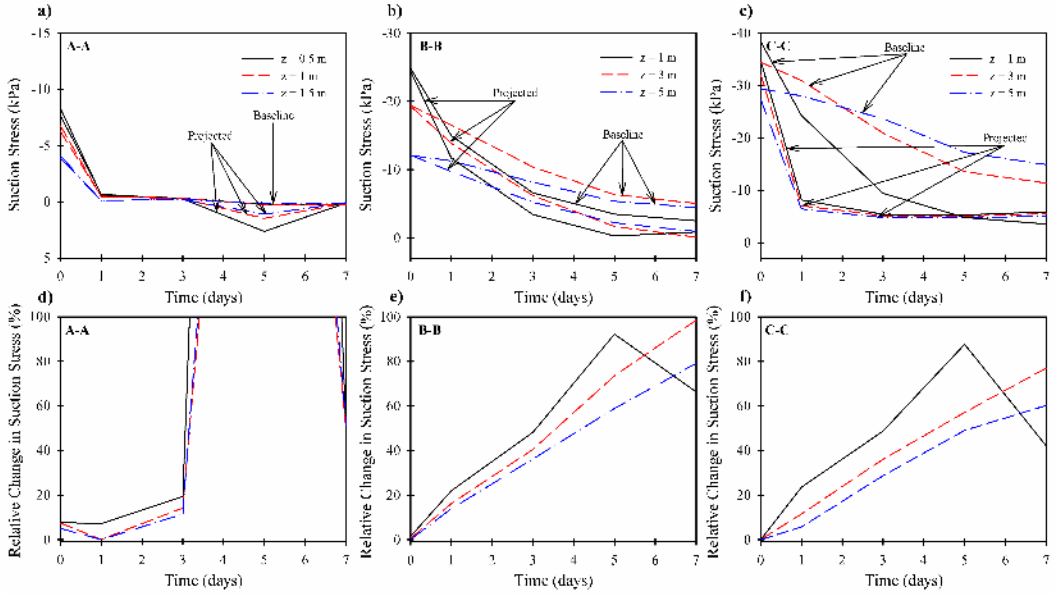


Figure 14 Simulated suction stress ($\sigma^s$) and relative change between baseline and projected precipitation extremes.

The change in the simulated FS with time, as predicted per the SSR method, is illustrated in Figures 15a through 15c for the three cross sections. Figures 15d through 15f show the relative percent changes in FS between the baseline and projected rain intensities. A positive change represents an increase in FS from the stationary to the nonstationary condition, whereas a negative change indicates merely the opposite. As can be seen, FS in cross-sections A-A and B-B never reaches the limit state, indicating that these sections within the slope remain stable. The low FS exhibited at the toe can possibly mean that the slope is near the brink of failure. The upper slope (i.e., cross-section C-C) appears to be unstable (i.e., FS < 1) under the nonstationary condition at just

t = 3.5-days, for z = 1 m below the infiltration boundary. Such behavior can be accredited to the rapid decrease in the shear resistance along the slip surface resulting from the large increase in the pore-water pressure under the nonstationary condition.

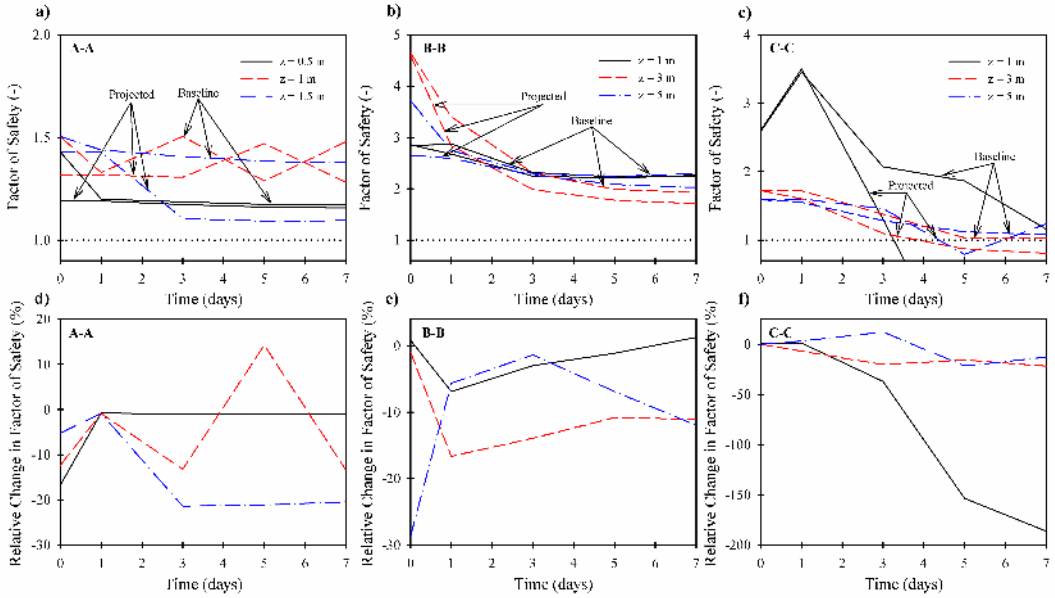


Figure 15 Simulated factor of safety (FS) and relative change between baseline and projected precipitation extremes.

Figure 16 depicts the pore-water pressure field in the slope at different times under the stationary condition. Before the 7-day heavy rainfall commences, the pore-water pressures under the initial condition vary almost linearly behind the infiltration boundary up to the depth of the water table and are more or less perpendicular to the slope surface. Once the 7-day heavy rain is imposed along the infiltration boundary of the slope, the pore pressure contours exhibit a lens shape, indicating that the pore pressure is smallest at z = 0 m. Once the 7-day heavy-rain ends, the rain intensity is equal to the initial conditions (i.e., annual historical rain) to bring the slope to a steady-state. As a

result, it can be seen that the negative pore-water pressures still contribute to the stability of the slope at t = 15 days.

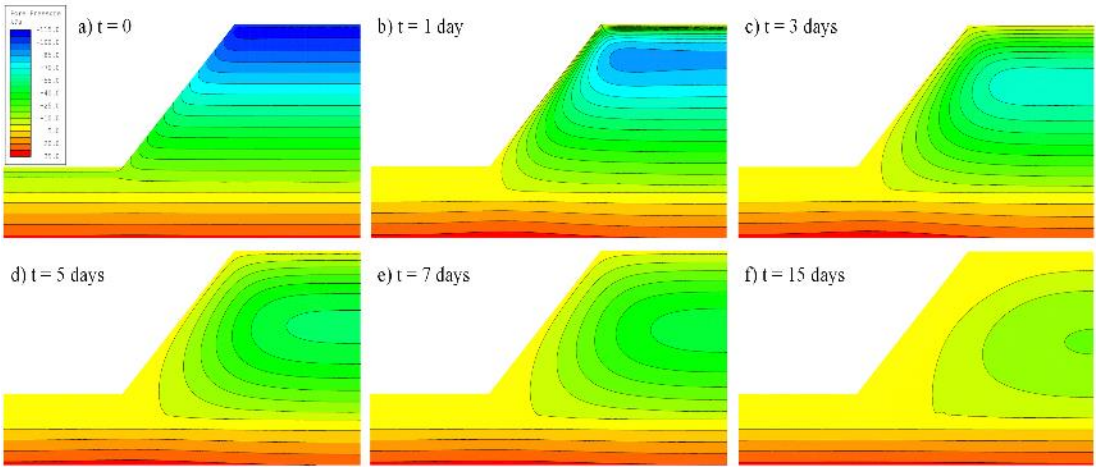


Figure 16 Contours of simulated pore water pressure at different times under baseline rainfall.

Figure 17 displays the pore-water pressure field in the slope at different times under the nonstationary condition. The shape of the wetting front in the first few meters below the upper slope boundary is most likely a manifestation of the projected rainfall intensity superseding the moisture holding capacity of the soil; similar behavior was seen under the baseline rainfall (Figure 16). After the heavy rainfall begins under the nonstationary condition, the pore-water pressure quickly increases. Additionally, Figure 17 demonstrates that the projected precipitation extreme, in comparison to the baseline extreme, has a more profound impact on the magnitude of the pore-water pressure and shape of the wetting front. For instance, the pore pressure contours under the nonstationary condition at t = 7 days are identical to those at t = 15 days under the stationary condition. In addition, Figure 17 shows that suction is no longer contributing to

the stability of the slope at t = 15 days. In fact, the pore-water pressure is approximately 5 kPa at t = 15 days under the projected rainfall. Such a significant increase in the pore-water pressure (i.e., more than a 100% increase from t = 0 to t = 15 days) can lead to a substantial reduction in the soil shear strength. Overall, the contours in Figure 17 tell us that the projected rain intensity increases the rate at which the wetting front progresses with depth, which can increase the probability of failure.

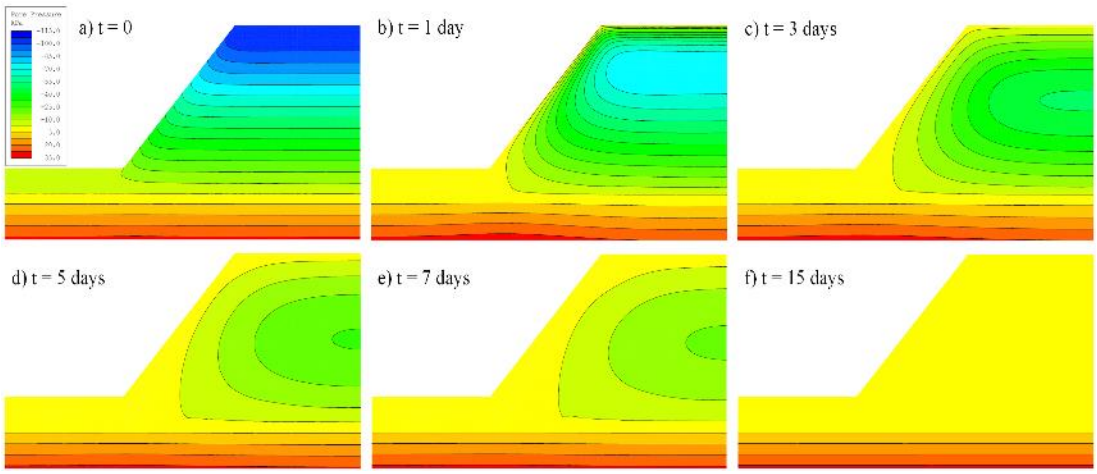


Figure 17 Contours of simulated pore water pressure at different times under projected rainfall.

Figure 18 demonstrates the impact of the imposed baseline rain intensity on the SRF. As can be seen, SRF are highest locally just above the toe of the slope for all of t, whereas the crest appears to become unstable at just t = 3 days. Beyond t = 3 days, the impacts of the imposed rain intensity become more apparent around the upper, middle, and lower slope boundaries. The contours near the infiltration boundary of the middle slope boundary follow a similar lens shape that is consistent with shallow landslides (e.g., Cruden and Varnes 1996).

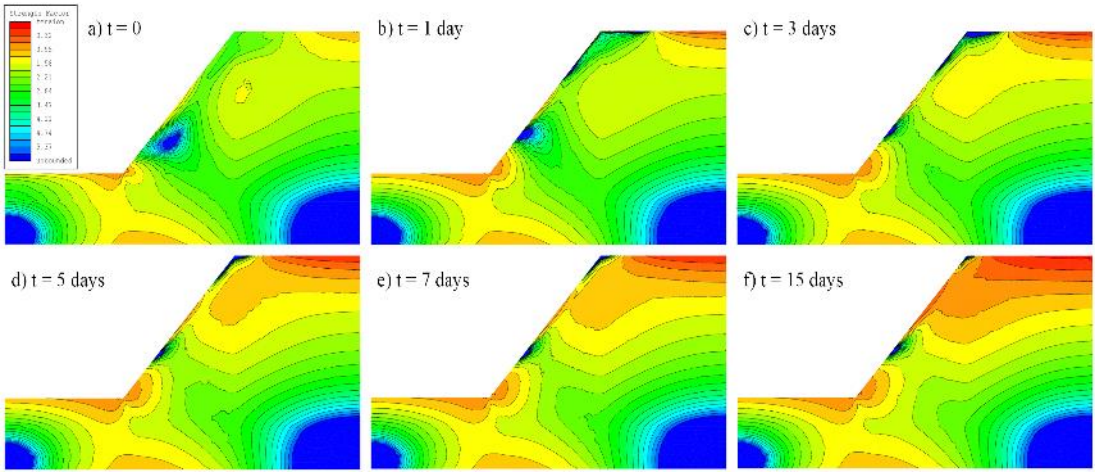


Figure 18 Contours of simulated strength reduction factor (SRF) at different times for the model slope under baseline precipitation extremes.

Figure 19 shows the SRF under the projected precipitation extremes. The slope appears to be stable under the initial conditions. Once the heavy rainfall commences at t = 1 day, tension (demonstrated by red zones in Figure 19) begins to develop within the middle and upper slope boundaries. As the projected rain persists up to approximately t = 3 days, the slope boundary approaches the limit state. Beyond t = 3 days, the amount of tension in the slope increases, which is indicative of active landsliding. In fact, the behavior of the contours around the middle slope boundary also follows a similar lens shape that is consistent with that observed from shallow landslides. In Figure 19, the increase in tension zone thickness with depth is a result of the quick advancement of the wetting front with time, which is in part due to the magnitude of the projected rainfall intensity and permeability of the soil. Moreover, the behavior of the middle slope for the nonstationary model shows a tension zone at t = 1 day, whereas the stationary model exhibits a similar tension zone 14 days later.

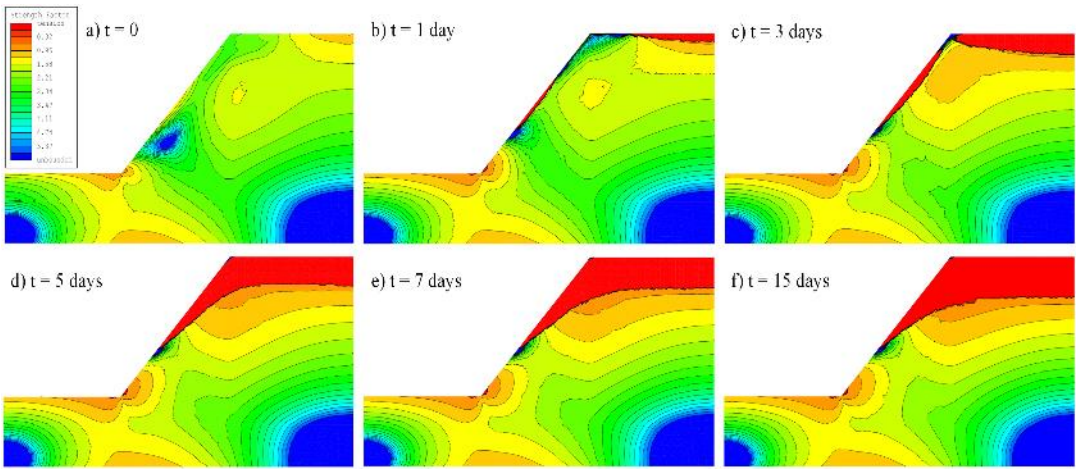


Figure 19 Contours of simulated strength reduction factor (SRF) at different times for the model slope under projected precipitation extremes.

The comparisons between the baseline and projected precipitation extremes were presented here for a natural earthen slope located in the Seattle region. Similar scenarios should also be considered for engineered slopes and earthen structures to assess their resilience under a changing climate. Generally, a higher rain intensity can expose an engineered slope or earth retaining structure to unprecedented increases in pore pressures. It leads to destabilization in such a slope or increases in active earth pressures behind the wall of a retaining structure. The goal of this study was to raise awareness regarding impacts that increased rain intensity in the future climate can have on not only natural slopes, but also engineered slopes and earth retaining structures. The study indicated that there is a need to reevaluate existing design and maintenance guidelines to ensure that our geotechnical structures can safely handle the extra load of water resulting from an increase in future rain intensity.

CHAPTER IV

# A THERMO-HYDRO-MECHANICAL FRAMEWORK COUPLING IMPACTS OF EXTREME DROUGHT ON SOIL STRENGTH

## Introduction

Quantifying the impacts of heat, vapor, and water transport on the mechanical properties of soils necessitates an innovative and conceptual thermo-hydro-mechanical framework defining soil strength as a function of concurrent variations in soil temperature and moisture. Doing so is not only critical in evaluating soil strength of partially saturated materials but also in the physics of land-surface processes on regional and global scales, particularly with respect to mass and energy fluxes between the terrestrial biosphere and atmosphere (Bittelli et al. 2008). Several works (e.g., de Vries 1963; Campbell et al. 1988; Lu and Dong 2015) have provided methods for analyzing the transfer of heat through partially saturated material. Lu and Dong (2015) provided a closed-form solution for thermal conductivity to evaluate conductive heat transfer in partially saturated soil. However, this method is limited to ambient temperatures ranging from 20 to 25 $^{o}$C and soil temperature typically varies between 0 and 20 $^{o}$C (e.g., Phillip and de Vries 1957). Other simplifying assumptions in existing mathematical models include, but are not limited to: constant vapor and saturated vapor pressure, invariant temperature, omission of condensation and evaporation, fixed tortuosity factor of 0.66, constant latent heat of vaporization, and fixed surface flux boundary conditions such as

heat and latent heat flux (e.g., Phillip and de Vries 1957; Cass et al. 1984; Fayer 2000; Fredlund and Rahardjo 2012). Several studies (e.g., Doorenbos and Pruitt 1977; Buck 1981; Henderson-Sellers 1984) have shown that each of the aforementioned metrics are transient in nature and can significantly impact the mechanical behavior of partially saturated soil.

This study proposes a unique framework to assess relationships between concurrent variations in soil temperature and moisture, leading to variations in soil strength. The ultimate goal of this framework is to understand the effects of the rate and variability of soil temperature and moisture change under a changing climate on the short- and long-term thermo-hydro-mechanical properties (e.g., shear strength) of soil. This is accomplished through the use of satellite soil moisture and temperature data, along with pertinent soil properties, obtained for a study area in the Sacramento-San Joaquin Delta (Delta), California. California's ongoing drought, along with the projected El Nino events, provides a unique opportunity to investigate the impacts of variations in soil moisture and temperature within the theoretical framework described in this research.

A technical validation of the proposed thermo-hydro-mechanical framework is provided by considering for a wide range of soil moistures and temperatures, surface flux boundary conditions (i.e., heat and latent heat flux), and soil textures (e.g., clay, sand, and silt).

## Derivation of Analytical Solution

The mathematical model applied to this framework was originally established by Fayer (2000) to assess heat and vapor flow through soils. This study extends Fayer's (2000) model to account for the impact of simultaneous variations in soil moisture and

temperature, over a wide range of surface flux boundary conditions, on the latent heat of vaporization, saturated vapor and vapor pressure, diffusivity of water vapor in air, relative humidity, and suction head.

The transport of heat through soils is of particular interests in complex engineering problems such as groundwater resource explorations, geological storage of radioactive waste, pavements, geothermal energy foundation systems, and carbon sequestration (e.g., Lu and Dong 2015; Tourchi and Hamidi 2015). Generally, there are two heat transfer mechanisms in soil: heat transfer through conduction and heat transfer through convection (e.g., Lu and Dong 2015). Furthermore, the transport of heat through soil based on the two aforementioned mechanisms can be delineated as follows:

$$q_h = -\lambda \nabla T + L q_v \tag{12}$$

where $q_h$ defines the heat flux density (W $m^{-2}$), $\lambda$ is the thermal conductivity (W $m^{-1}$ $K^{-1}$), $\nabla T$ is the temperature gradient (K $m^{-1}$), $L$ is the latent heat of vaporization of water (J $kg^{-1}$), and $q_v$ is the vapor flow (kg $m^{-2}$ $s^{-1}$). The first term on the right-hand side of Eq. 12 represents heat transfer through conduction (sensible heat) while the second term describes heat transfer by water vapor (latent heat flux) (e.g., Bittelli et al. 2008).

In Eq. 14, $L$ is most commonly treated as a constant however Henderson-Sellers (1984) showed that $L$ varies as a function of temperature. As a result, the latent heat of vaporization with variations in temperature is determined as:

$$L = 1.92 \times 10^6 \left[\frac{T}{(T-33.91)}\right]^2 \tag{13}$$

The fundamental equation used to compute the diffusion of water vapor in soil (i.e., convective heat transfer) is represented by Fick's Law of diffusion defined as:

$$q_v = -\frac{D}{\rho_w}\frac{\partial \rho_v}{\partial z} \quad (14)$$

where $q_v$ is the flux density of water vapor (cm $hr^{-1}$), $\rho_w$ is the density of liquid water (g $cm^{-3}$), $D$ is the vapor diffusivity in soil ($cm^2$ $hr^{-1}$), $\rho_v$ is the vapor density (g $cm^{-3}$), and $z$ is the depth, positive downward (cm). In order to make $q_v$ in Eq. 14 equivalent to that in Eq. 12, Eq. 14 should be multiplied by $\rho_w$. When implementing Fick's law to define vapor diffusion in soils, $D$ must be defined as follows:

$$D = \alpha(\theta_s - \theta)D_a \quad (15)$$

where $\alpha$ represents the tortuosity factor of the soil, the term ($\theta_s - \theta$) is the air – filled porosity (dimensionless), where $\theta_s$ and $\theta$ are the saturated and volumetric water contents, respectively, and $D_a$ is the diffusivity of water vapor in air ($cm^2$ $s^{-1}$). For simplicity, the tortuosity factor, $\alpha$ is typically fixed to 0.66 under isothermal flow conditions. However, $\alpha$ can be delineated as a function of the pore-water saturation ($S$) and pore size distribution ($n$) as follows:

$$\alpha = \beta^{\frac{2}{3}} = [(1 - S)n]^{\frac{2}{3}} \quad (16)$$

where $\beta$ is the cross-sectional area of the soil available for non-isothermal water vapor flow.

From Eq. 15, $D_a$ is typically held fixed (e.g., Fayer 2000) however, Kimball et al. (1976) showed that $D_a$ is temperature dependent and as a result is determined as:

$$D_a = 0.229\left[1 + \frac{T}{273}\right]^{1.75} \times 10^{-4} \quad (17)$$

where $D_a$ is in $m^2\ s^{-1}$ and Eq. 17 shows that the diffusivity of water vapor in air is intrinsically temperature dependent (e.g., Kimball et al. 1976).

Fick's law, as defined by Eq. 14, can be explicitly written to include gradients for soil suction head ($h$) and temperature by using the chain rule of differentiation:

$$q_v = -\frac{D}{\rho_w}\frac{\partial \rho_v}{\partial h}\frac{\partial h}{\partial z} - \frac{D}{\rho_w}\frac{\partial \rho_v}{\partial T}\frac{\partial T}{\partial z} \tag{18}$$

where $q_v$ presented here is still in units of cm $hr^{-1}$. As previously noted, Eq. 18 can be multiplied by $\rho_w$ which yields the following expression:

$$(\rho_w)q_v = -D\frac{\partial \rho_v}{\partial h}\frac{\partial h}{\partial z} - D\frac{\partial \rho_v}{\partial T}\frac{\partial T}{\partial z} \tag{19}$$

where the term of the left-hand side of eq. 19 ($\rho_w\ q_v$) characterizes the vapor flow (g $cm^{-2}$ $hr^{-1}$) and can be incorporated into Eq. 12 to explicitly define heat transfer through soils.

The vapor density, $\rho_v$ at a definitive point can be defined as a function of the saturated vapor density ($\rho_{vs}$) and relative humidity ($H_R$) as follows:

$$\rho_v = \rho_{vs} H_R \tag{20}$$

Because the water vapor density is a function of relative humidity and temperature, Eq. 18 can be rewritten. Furthermore, combining Eqs. 18 and 20, using the product rule for differentiation and assuming that the change in $H_R$ with respect to variations in temperature is zero (i.e., $\partial H_R/\partial T = 0$), Fick's Law can be presented as follows (e.g., Fayer 2000):

$$q_v = -\frac{D}{\rho_w}\rho_{vs}\frac{\partial H_R}{\partial z} - \frac{D}{\rho_w}H_R\frac{\partial \rho_{vs}}{\partial T}\frac{\partial T}{\partial z} \tag{21}$$

The first term on the right-hand side of Eq. 21 explicitly represents isothermal vapor diffusion, whereas the second term presents thermal vapor diffusion. From the soil suction head, the relative humidity of the soil can be defined as:

$$H_R = \exp\left[-\frac{hMg}{RT}\right] \tag{22}$$

where $M$ is the molecular weight of water (~18 g $mol^{-1}$), $g$ is the gravitational acceleration constant (cm $s^{-2}$), and $R$ is the gas constant ($8.314 \times 10^7$ erg $mol^{-1}$ $K^{-1}$).

Several works have been published which suggest that Eq. 21 underestimates the temperature gradients within the air phase of the soil pores (i.e., vapor diffusion). In light of this finding, Philip and deVries (1957) proposed adding an enhancement factor ($\eta$) to the thermal vapor diffusion term presented in Eq. 21. In detail, they state that $\eta$ implicitly accounts for the transfer of vapor in the liquid phase through pores by considering for condensation and evaporation processes. In light of this adjustment, as well as expressing the $H_R$ gradient in terms of the suction gradient ($\partial h/\partial z$), a modified form of Eq. 21 can be defined as follows:

$$q_v = \left(\frac{D}{\rho_w}\rho_{vs}\frac{Mg}{RT}H_R\frac{\partial h}{\partial z}\right) - \left(\frac{D}{\rho_w}\eta H_R\frac{\partial \rho_{vs}}{\partial T}\frac{\partial T}{\partial z}\right) \tag{23}$$

Eq. 23 explicitly considers the effect of temperature gradients and enhanced vapor diffusion in soils. The parameters in the first term on the left hand side of Eq. 23 can be combined to yield "isothermal vapor conductivity" as a function of the soil suction gradient. Similarly, the second term on the left hand side delineates the "non-isothermal vapor conductivity" as a function of the temperature gradient. Substituting Eq. 23 back into Eq.14, we achieve the following expression:

$$q_h = -\lambda \nabla T + L\left[\left(D\rho_{vs}\frac{Mg}{RT}H_R\frac{\partial h}{\partial z}\right) - \left(D\eta H_R\frac{\partial \rho_{vs}}{\partial T}\frac{\partial T}{\partial z}\right)\right] \quad (24)$$

In order to delineate the impact of concurrent variations in soil temperature and moisture on the soil suction head, Eq. 24 can be solved for *h*. As such, Eq. 22 must first be substituted into Eq. 20, yielding the following expression:

$$h = -\ln\left(\frac{\rho_v}{\rho_{vs}}\right)\frac{RT}{Mg} \quad (25)$$

and now Eq. 25 can be rewritten as follows:

$$q_h = -\lambda \nabla T + LD\rho_{vs}\frac{Mg}{RT}\exp\left[\frac{RT}{Mg}\ln\frac{\rho_v}{\rho_{vs}}\frac{Mg}{RT}\right]\frac{\partial h}{\partial z} - LD\eta\exp\left[\frac{RT}{Mg}\ln\frac{\rho_v}{\rho_{vs}}\frac{Mg}{RT}\right]\frac{\partial \rho_{vs}}{\partial T}\frac{\partial T}{\partial z} \quad (26)$$

Simplifying Eq. 26 yields the following:

$$q_h = -\lambda\frac{\partial T}{\partial z} + LD\rho_{vs}\frac{Mg}{RT}\frac{\rho_v}{\rho_{vs}}\frac{\partial h}{\partial z} - LD\eta\frac{\partial \rho_{vs}}{\partial T}\frac{\partial T}{\partial z} \quad (27)$$

where *h* in Eq. 27 can be solved for directly through integration:

$$\int_z q_h = -\int_z \lambda\frac{\partial T}{\partial z} + \int_z LD\rho_{vs}\frac{Mg}{RT}\frac{\rho_v}{\rho_{vs}}\frac{\partial h}{\partial z} - \int_z LD\eta\frac{\partial \rho_{vs}}{\partial T}\frac{\partial T}{\partial z} \quad (28)$$

After integrating Eq. 28, the following analytical solution is obtained:

$$q_h = \frac{1}{z}\left[-\lambda T + LD\rho_{vs}\frac{Mg}{RT}\frac{\rho_v}{\rho_{vs}}h - LD\eta\frac{\partial \rho_{vs}}{\partial T}T\right] \quad (29)$$

Solving Eq. 29 for *h*, yields an analytical solution that delineates the coupled effects of heat, water vapor, and heat flux on the one-dimensional, non-isothermal suction head as such:

$$h = \frac{q_h zRT + \lambda RT^2}{LD\rho_v Mg} + \frac{\eta RT^2}{\rho_{vs}Mg}\frac{\partial \rho_{vs}}{\partial T} \quad (30)$$

The thermal conductivity, $\lambda$ of the soil can be quantified indirectly from direct measurements of $q_h$, the latent heat flux ($q_l$), and $\nabla T$ is as follows:

$$\lambda = -\left(\frac{q_h - q_l}{\nabla T}\right) \tag{31}$$

Doorenbos and Pruitt (1977) provided an empirical equation to calculate saturated vapor pressure as a function of temperature. The empirical equation for $\rho_{vs}$ (g/cm$^3$) is represented as follows:

$$\rho_{vs} = \exp\left[A - \frac{B}{T} - C \ln T\right] \tag{32}$$

where the coefficients *A*, *B*, and *C* are equal to 46.44, 6790.5, and 6.03, respectively.

It is noted that Eq. 32 tends to overestimate values for $\rho_{vs}$ and, thus will provide overestimations for the nonisothermal suction head. As such, this study employed optimization using the method of least squares to determine values of *A*, *B*, and *C* which better correlate to measured data. In order to alleviate any bias, a *feasible – path* method was used to start the solution with an estimate of optimum points for *A*, *B*, and *c*. Various *A*, *B*, and *C* coefficients were then evaluated using an iterative refinement. When the sum of the squared residuals (i.e., square of the difference between predicted and measured values) was at its minimum, feasibility was maintained and the resulting solutions for *A*, *B*, and *C* were taken as the optimum points. The optimum coefficients characterizing *A*, *B*, and *C* for the empirical function representing $\rho_{vs}$ were selected as 45.15, 6768.8, and 8.2, respectively.

The partial derivative of $\rho_{vs}$ with respect to variations in $T$ is defined as:

$$\frac{\partial \rho_{vs}}{\partial T} = \rho_{vs}\left[\frac{B}{T} - C\right]\frac{1}{T} \tag{33}$$

It is noted that, the first term on the right-hand side of Eq. 23 represents the isothermal flux. However, the addition of Eq. 32 into Eq. 23 does allow once to implicitly simulate the effects of varying soil temperature on $\rho_{vs}$ and consequently, the soil suction head.

The vapor density, $\rho_v$ as it appears in Eq. 30 is inherently temperature dependent and therefore can be delineated as such:

$$\rho_v = \frac{1.4\exp\left[A - \frac{B}{T}\right]}{z} \tag{34}$$

where $\rho_v$ is presented here in units of g/cm$^3$; T and z are in K and z, respectively, and the coefficients describing $A$ and $B$ are 20.39 and 5132, respectively. Similar to behavior of Eq. 32 representing $\rho_{vs}$, Eq. 34 tends to over-predict $\rho_v$ by some factor. In light of this, a new set of coefficients for $A$ and $B$ from Eq. 34 were determined using the method of least squares optimization. A similar approach was used here as that discussed earlier on for Eq. 32. The proposed optimum coefficients describing $A$ and $B$ for the empirical function representing $\rho_v$ are 20.17 and 5111.9, respectively.

The *dependence* of a response metric such as the soil suction head is presented here as a function in which an environmental trend, like temperature, acts as a driving variable [i.e., $h = f(T)$] (e.g., Sierra et al. 2015). The *intrinsic sensitivity* of $h$ with respect to an environmental trend such as $T$ can be characterized by the partial derivative of $h$

with respect to T. Thus, the intrinsic temperature sensitivity of the non-isothermal suction head presented in Eq. 30 can be defined as follows:

$$\frac{\partial h}{\partial T} = \frac{\partial}{\partial T}\left(\frac{q_h(z)RT+\lambda RT^2}{LD\rho_v Mg} + \frac{\eta RT^2}{\rho_{vs} Mg}\frac{\partial \rho_{vs}}{\partial T}\right) \quad (35)$$

where $\partial h/\partial T$ can be used to make a definitive distinction between the dependence and sensitivity of the soil suction with respect to changes in soil temperature. The *intrinsic sensitivity* characterized through the partial derivative is a measurement of the absolute change in the response variable with respect to changes in the driving variable (e.g., Davidson et al. 2012; Sierra et al. 2015). As such, the *intrinsic sensitivity* of *h* with changes in *T* is characterized as follows:

$$\frac{\partial h}{\partial T} = \frac{q_h zR+2\lambda RT}{LD\rho_v Mg} + \frac{2\eta RT}{Mg} \quad (36)$$

where the *intrinsic* temperature sensitivity of the non-isothermal soil suction head is in units of cm $K^{-1}$. Furthermore, Eq. 36 may be used to effectively demonstrate that mechanistic processes in soils can be intrinsically temperature sensitive.

**Non-isothermal Shear Strength of Unsaturated Soils**

A variety of technical authorities such as geotechnical, geoenvironmental, and agricultural engineers, as well as soil scientists, are interested in understanding the shear strength of unsaturated soils (e.g., Fredlund and Vanapalli 1996; Lu and Likos 2004). The shear strength of soils is required to address a number of complex engineering problems including foundation design, slope stability, pavement design, lateral earth pressure, and the resistance to traction and tillage for agricultural applications (e.g., Fredlund and Vanapalli 1996).

The shear strength of soil can be defined best as the maximum resistance per unit area the soil is capable of supporting external compressive loads (e.g., Lu and Likos 2004). Most of the soils that stabilize our foundation systems, earthen retaining structures, and roadways, and play a vital role in food production, are in an unsaturated condition. Unsaturated soils also play an important role for the water balance and matter transport between the terrestrial biosphere and atmosphere. Soils in an unsaturated state have negative pore water pressures (e.g., Fredlund and Vanapalli 1996; Lu and Likos 2004). Shear strength is not constant for unsaturated soils and, thus depends on soil saturation and negative pore water pressure (or matric suction) (Vahedifard et al. 2015). In addition, the magnitude of shear strength can vary substantially under a wide range of saturations and matric suctions and, thus can have a significant impact of the stability of our critical infrastructure.

The shear strength of an unsaturated soil can be captured using the suction stress. The suction stress collectively represents the thermodynamic inter-particle free energy, where, in any thermodynamic system, the free energy is the portion of first-law internal energy that is available to perform work. The inter-particle free energy can exists in the form of physico-chemical forces such as van der Waals forces, electrical double-layer forces, and chemical cementation forces at the grain contacts, surface tension forces, and forces arising from negative pore water pressure (Lu and Likos 2006). Physico-chemical forces only exist in fine-grained soils (e.g., clay) and can vary significantly over a wide range of soil moistures and temperatures. In contrast, the inter-particle forces occurring at the air-water interfaces where surface tension exist are the only suction stress component in coarse grained soils (e.g., sand).

Lu and Likos (2006) used the suction stress to capture changes in the effective stress under both saturated and unsaturated isothermal conditions as follows:

$$\sigma' = \sigma - u_a - \sigma^s \tag{37}$$

where $\sigma'$ represents the effective stress, $\sigma$ represents the total stress, $u_a$ is the pore air pressure, and $\sigma^s$ defines the suction stress. The effective stress can be conceptualized as the force that keeps an assemblage of particles rigid. A higher effective stress results in larger shear strength and less chance of structural instabilities such as bearing capacity failure, differential settlement, slides, or flows in any infrastructure.

The suction stress is used to quantify impacts of soil suction and saturations on the effective stress and corresponding shear strength. It is noted that suction stress is a collective representation of the work arbitrated by thermal energy. Therefore, suction stress is intrinsically temperature sensitive and should be explicitly defined as a function of temperature. This study uses a new solution representing the nonisothermal matric suction to extend Bishop's (1959) effective stress model representing changes in soil suction and saturation as follows:

$$\sigma^s = -S_e(u_a - u_w)^T \tag{38}$$

where $S_e$ represents the effective degree of saturation (or normalized water content) and $(u_a\text{-}u_w)^T$ is the nonisothermal matric suction for an intact soil mass. The effective degree of saturation is used to capture the contribution of the suction stress in an unsaturated soil matrix due to the coupled effects of matric suction and surface tension (Lu et al. 2010). Using van Genuchten (1980) - Mualem's (1976) model, along with the proposed solution

for the nonisothermal matric suction, $S_e$ can be expressed in the following form (Lu et al. 2010):

$$S_e = \left\{\frac{1}{1+[\alpha(u_a - u_w)^T]^n}\right\}^{1-\frac{1}{n}} \quad (39)$$

where $\alpha$ and $n$ are fitting parameters delineating the relationship between matric suction and soil saturation. As defined, $\alpha$ approximates the inverse of the air-entry pressure and $n$ symbolizes the distribution of the soil's pore size. The air-entry pressure represents the point at which air is pushed out of a soil's pore space (i.e., the system approaches saturation). In general, fined-grained soils, in comparison to coarse-grained soils, support larger air-entry pressures and consequently, higher matric suctions (Lu et al. 2010).

From Eqs. 38 and 39, the matric suction is defined as a function of the nonisothermal soil suction head ($h$) and unit weight of water as follows:

$$(u_a - u_w)^T = -\frac{h}{\gamma_w} \quad (40)$$

where $\gamma_w$ is the unit weight of water.

The unified effective stress theory presented in Eq. 37 can be used to define the shear strength of unsaturated soils as:

$$\tau = c' + [(\sigma - u_a) - \sigma^s]\tan\phi' \quad (41)$$

where $\tau$ symbolizes the shear strength, $c'$ is the effective cohesion intercept which is theoretically zero for coarse-grained soils and greater than zero for fine-grained soils, the difference $(\sigma - u_a)$ delineates the net normal stress, and $\phi'$ is the effective friction angle. Generally, coarse-grained soils exhibit greater values of $\phi'$.

## Data Acquisition

The soil moisture and temperature data implemented in this work is collected from the North America Land Data Assimilation System (NLDAS), as a part of the Goddard Earth Sciences Data and Information Services Center (GES DISC). The NLDAS integrates a large quantity of observed data and model reanalysis data to drive offline land-surface models (LSMs) (Rui and Mocko 2014). In addition, the NLDAS executes at a 1/8° grid spacing over central North America, enabled by the Land Information System (LIS).

The LSM employed in the study was that developed through the United States National Oceanic and Atmospheric Administration (NOAA). For the current study, soil data is acquired from January 1, 2006 through August 31, 2015, over four vertical layers 0-10, 10-40, 40-100, and 100-20 cm. The extent of the data is 37.5005 to 39.3755 N and -122.7505 to -120. 8675 W, which encompasses all of the Sacramento-San Joaquin Delta (Delta), California. Further, the acquired data is displayed as a grid with a spatial resolution of approximately 0.125 degrees.

The distributions and statistics summary of the driving variables representing soil moisture, soil temperature, and heat flux as obtained through the NLDAS are illustrated in Figs. 20, 21, and 22, respectively. The soil moisture, as presented in Figure 20, represents the weighted average from 0-200 cm depth of soil below the ground surface. The boxplot shows the median (top mark), mean (bottom mark), and 25$^{th}$ (lower edge) and 75$^{th}$ (upper edge) percentiles. The 5$^{th}$ and 95$^{th}$ percentiles are represented by the upper and lower circles, respectively. It has been noted that California has been undergoing an extreme drought since 2012. As can be seen in Figure 20, the average soil

moisture (bottom mark) for each month shows an apparent decrease from the commencement of the drought in April 2012 up through August 2015. In detail, the soil moisture decreases approximately 92% from December 2012 to August 2015.

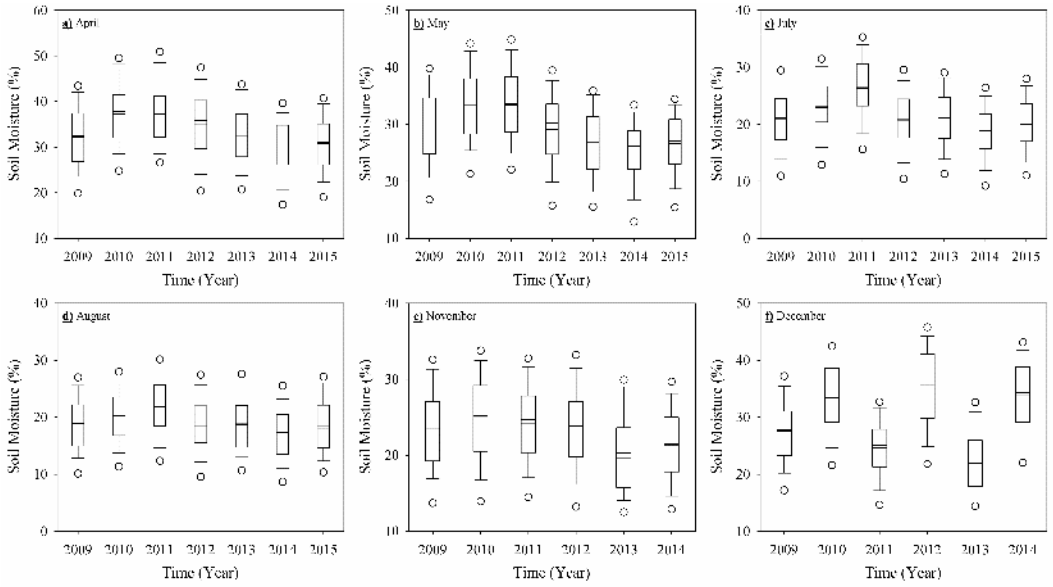


Figure 20 Distribution of soil moisture (%)for the Sacramento-San Joaquin Delta, California.

The soil temperature (˚C) depicted in Figure 21 represents the weighted average from 0-200 cm depth of soil below the ground surface. The boxplot shows the median (top mark), mean (bottom mark), and 25$^{th}$ (lower edge) and 75$^{th}$ (upper edge) percentiles. The 5$^{th}$ and 95$^{th}$ percentiles are represented by the upper and lower circles, respectively. As displayed in Figure 21, the average soil temperature for each month shows an apparent increase from the start of the drought in April 2012 up through August 2015. The greatest relative percent increase in the soil temperature (i.e., about 3.5% increase)

occurred from December 2012 to August 2015, which so happens to be the period of the highest decrease in soil moisture (see Figure 20).

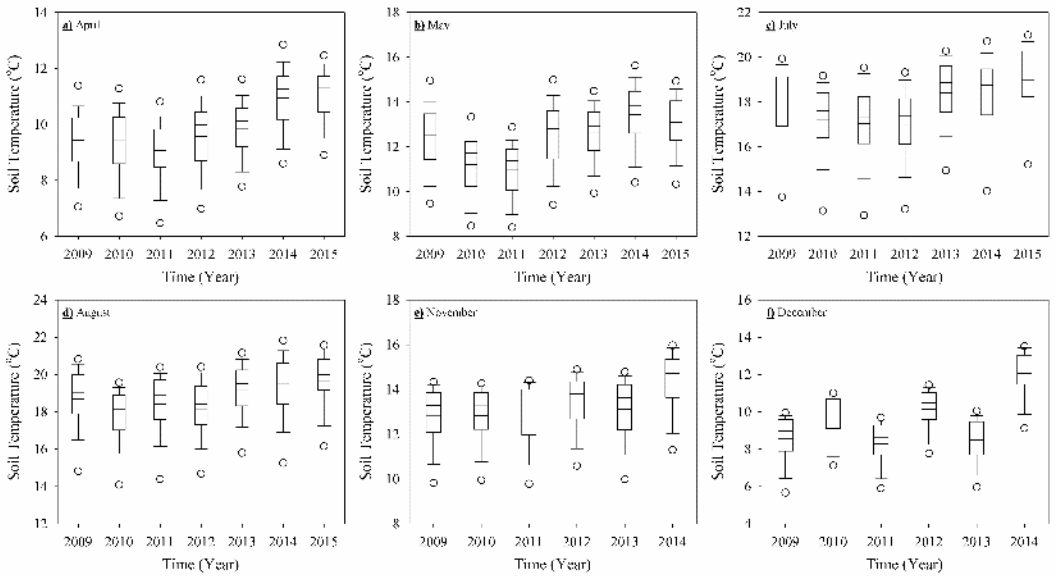


Figure 21 Distribution of soil temperature (˚C) for the Sacramento-San Joaquin Delta, California.

The heat flux (˚C) displayed in Figure 21 represents the instantaneous average heat flux at the ground surface. The heat flux is defined as being positive in the upward direction and negative downward. The boxplot shows the median (top mark), mean (bottom mark), and 25$^{th}$ (lower edge) and 75$^{th}$ (upper edge) percentiles. The 5$^{th}$ and 95$^{th}$ percentiles are represented by the upper and lower circles, respectively. In Figure 21, the average surface heat flux was at a maximum in May of 2009 and a minimum in December 2010. There was a distinct 31% increase in the heat flux from April. It can be deduced from Figure 21 that the soil temperature may have had some impact on the rate at which heat was being transferred through the soil's pore space.

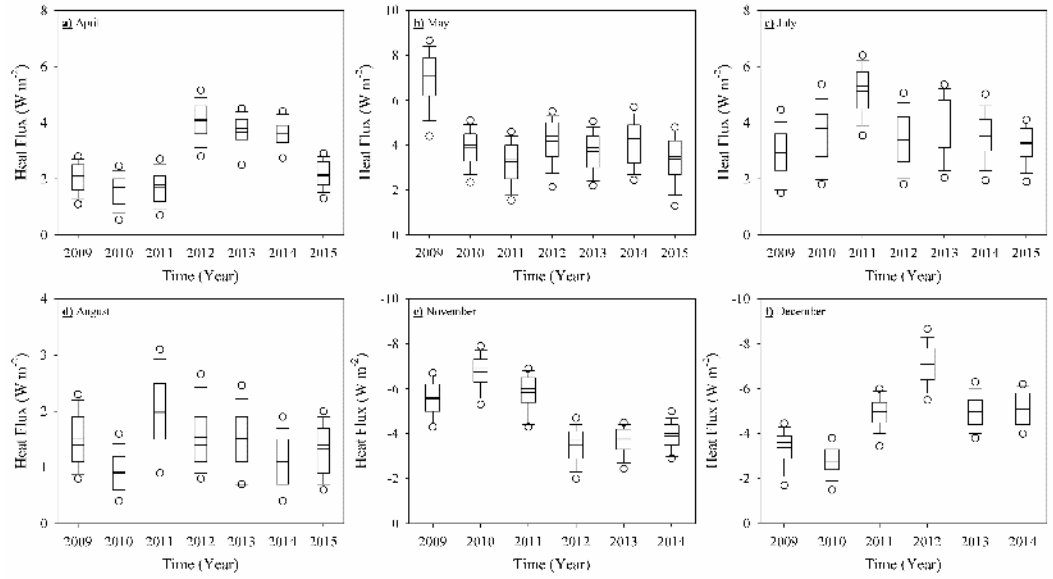


Figure 22 Distribution of surface heat flux (W $m^{-2}$) for the Sacramento-San Joaquin Delta, California.

## Verification of Analytical Solution

In order to investigate the validity of analytical solution representing the non-isothermal soil suction head (Eq. 32), the following section associates predicted versus measured values of the latent heat flux ($q_l$), where $q_l$ is defined by the product of the latent heat of vaporization (Eq. 15) and vapor flow (Eq. 21). The correlation between predicted and measured values is defined in terms of the corresponding root mean squared error (*RMSE*).

The correlation between the predicted and measured latent heat flux is illustrated for 184 data points, across four discrete areas (as indicated by the Lon. and Lat. in each subfigure), in Figure 23 along with the corresponding value of *RMSE*. It can be deduced from Figure 23 that the product of Eq. 32 and Eq. 15 predicts $q_l$ rather well. Moreover,

the values of *RMSE* in Fig.23 indicate that the variability in the measured data representing $q_l$ is captured well by the proposed predictive equation.

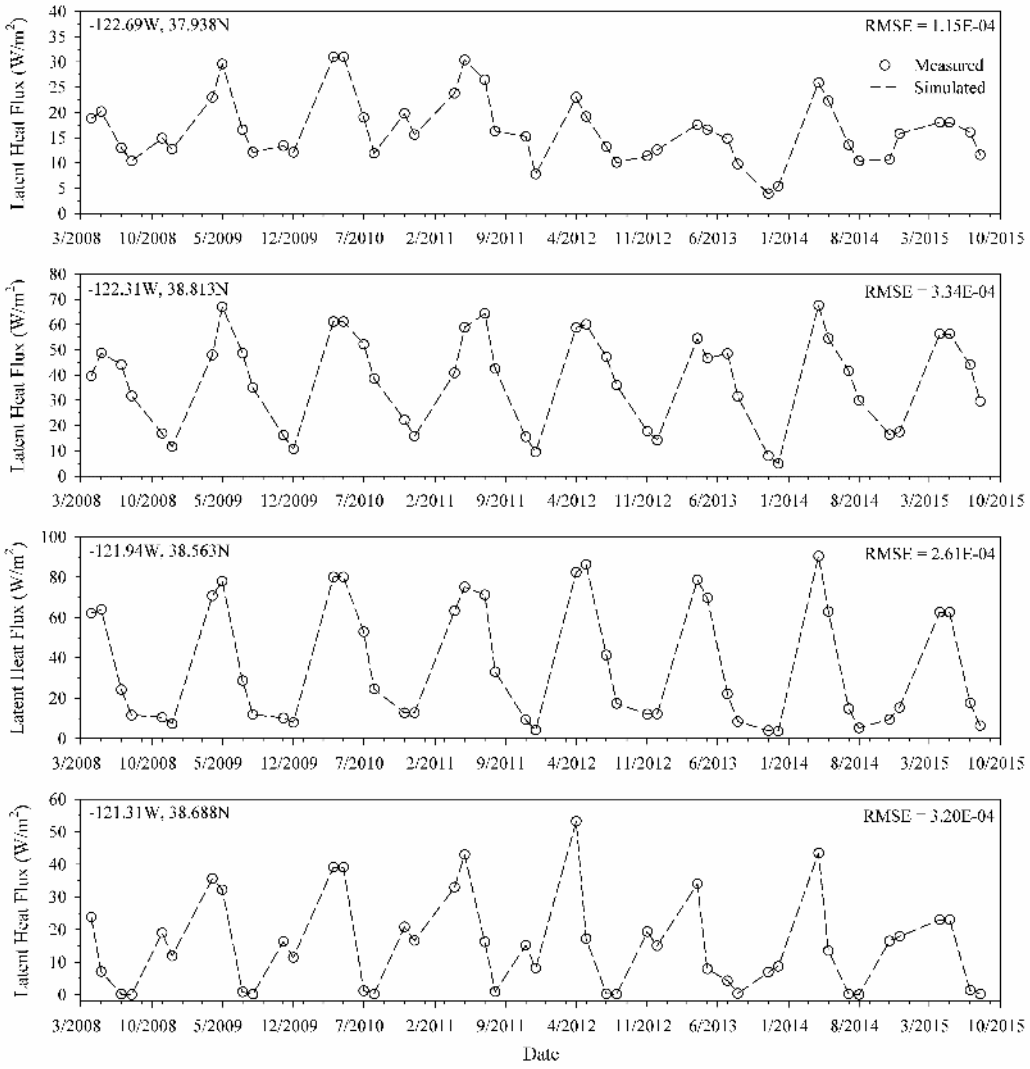


Figure 23 Predicted versus measured latent heat flux ($q_l$).

\

# CHAPTER V

# CONCLUSION

## Summary of work accomplished for assessing drought-induced weakening mechanisms imposed on California's levees under multiyear extreme drought

The purpose of this work was to discuss and highlight the critical need for quantitatively assessing the resilience of California's earthen levees to the ongoing extreme drought. California's drought could adversely impact its already at-risk levee system, especially if it is followed by heavy rainfall-induced flooding, as seen in several previous drought events. Drought-induced weakening mechanisms such as soil strength reduction, desiccation cracking and soil softening, land erosion and subsidence, soil organic carbon decomposition can add even more complexity to an already challenging problem. As demonstrated by previous failures which occurred under similar drought events, these processes can prompt several modes of earthen levee failures such as overtopping, slumping, and sliding. So, there is a serious need to improve our current state of knowledge about the drought-induced threats and take subsequent actions in a timely manner to strengthen our levee systems.

Assessing the impacts of climate change on levees could be conducive in answering critical questions, including the following: (I) How does drought influence the failure probability in the current and future states of levees? (II) How does the rate and variability of drought affect the short and long term behavior of California's levees? (III)

What are the limitations in existing levee design, maintenance, and monitoring guidelines with respect to extreme loads resulting from drought, flooding, increased rainfall-intensity, earthquake, and temperature rise? (IV) What are the adaptation and mitigation strategies for reducing drought impacts on the performance of levee systems throughout California? The geotechnical engineering community can take a proactive role to properly answer the above – listed questions and protect the health and welfare of the general public.

In the current hydrologic and geotechnical design guidelines, drought risk and the impacts of potential future climate changes have not been considered (Vahedifard et al. 2015a). Given the significance of projected changes, there is a need to develop a framework for integrating drought and climate change risks in engineering design. Assuring the resilience of the California's levees in a prolonged drought involves many administrative and complex technical aspects, and necessitates the development of appropriate strategies and measures that are effective and efficient on both the short and long term.

In March 2015, Gov. Jerry Brown of California proposed to accelerate more than $1 billion in water resource spending. More than 65% of the proposed budget is anticipated to go towards rehabilitating flood control structures (e.g., levees) with hopes of increasing their resilience under an extreme condition such as drought. This is an example of forward looking strategy to be more prepared for the future. Further, different authorities are constantly monitoring the Delta levees to address and repair distressed levee sections. However, more in-depth scientific research is needed to understand how

drought can threaten the integrity of critical infrastructure such as levees, especially under a multi-hazard scenario.

**Summary of work accomplished for quantifying the impact of historical and future precipitation extremes under a changing climate on slope stability**

An increase in the statistics of extremes (e.g., increased rainfall intensity) due to a changing climate highlights the need to quantify the effects of these extremes on the resilience of natural and engineered earthen slopes. Increased rainfall intensity can escalate the pore-water saturation in unsaturated soils leading to significant reductions in the soil suction and consequently, soil strength. The aim of this study was to quantitatively compare the influence of stationary (historical) and nonstationary (future) Intensity-Duration-Frequency (IDF) curves obtained for the Seattle area on the stability of a natural earthen slope. The stationary and nonstationary IDF curves were implemented into a series of fully coupled 2D transient unsaturated seepage finite element simulations. A homogenous silty soil slope along with the soil-water characteristic curve and hydraulic conductivity function were used to define the soil material properties. The mechanical behavior of the modeled slope at a 7-day rainfall duration obtained for a 50-year recurrence interval were compared in terms of factor of safety, displacements, matric suctions, degrees of saturation, and suction stresses.

The FE simulations indicated that the use of historical precipitation extremes, in comparison to future extremes, can lead to significant overestimation in the slope performance, which is affected by increased transient seepage rates. The upper boundary of the model slope showed very poor performance under historical and projected rainfall conditions. However, the slope performance under the future climate was substantially

less than that under the stationary historical condition. Additionally, the historical and projected precipitation extremes, analyzed using a stationary and nonstationary assumption, resulted in a lens failure mechanism that is consistent with that shown by shallow landslides. The results demonstrated the need for proper consideration of the impacts of extreme precipitation events under a changing climate in the analysis, maintenance, and monitoring of natural slopes.

**Summary of work accomplished for the proposed thermo-hydro mechanical framework delineating soil suction with variations in soil moisture and temperature, under various surface flux boundary conditions**

This study proposed a conceptual thermo-hydro-mechanical framework delineating soil suction with variations in soil temperature and moisture, under various surface flux boundary conditions. The soil moisture and temperature data implemented in this work was obtained from the North America Land Data Assimilation System (NLDAS), as a part of the Goddard Earth Sciences Data and Information Services Center (GES DISC).

The soil data was acquired over a study period from January 1, 2006 through August 31, 2015. The data was representative of four distinct vertical layers soil layers: 0-10, 10-40, 40-100, and 100-20 cm. The extent of the data was 37.5005 to 39.3755 N and -122.7505 to -120. 8675 W, covering a study area founded in Sacramento-San Joaquin Delta (Delta), California. The significance of the selected study area was its ongoing extreme drought and its historical and forthcoming El Niño events.

The proposed framework showed good agreement with observed values representing a wide range of latent heat flux ($q_l$), for a study area in the Sacramento-San Joaquin Delta, California region. Values of the normalized root mean squared error were

provided to evaluate the variation between the predicted and measured $q_l$, over a wide range of soil moistures and temperatures. In detail, the proposed method forecast $q_l$ rather well for a wide range of measured $q_l$.

The new analytical approach only requires two controlling variables (i.e., soil moisture and temperature) and can be implemented to provide an accurate and practical framework to analyze soil suction for a variety of soil types (i.e., clay, sand, and silt) under extreme events such as extreme drought. The proposed method presents a useful tool for explaining true behavior of soil suction over a wide range of soil moisture and temperature. However, great caution must be taken in counting on soil suction for defining soil shear strength due to uncertainties associated with and huge variation of suction with time.

**Recommendations for future research**

The data used to compare against the thermo-hydro-mechanical (THM) framework representing the non-isothermal soil suction head will be implemented in future research to quantify the suction stress within the first two meters of depth of soil for the California Delta. The interactive energy consumed by suction stress can exist in the form of van der Waals forces, electric double-layer forces, surface tension, and solid-fluid interface forces resulting from pore water pressure (e.g., Lu et al. 2010). These thermodynamic free energy forces collectively represented by the suction stress provide the extent of work needed to keep an assemblage of soil particles rigid, which provides soil with resistance to external compressive and tensile forces (i.e., soil strength). Lu et al. (2009) and (2010) showed that the non-monotic variation in soil shear and tensile strengths occurs at soil saturations less than and greater than 20% and

80%. The non-isothermal suction stress as predicted per the proposed THM framework will then be used to capture variations in soil shear strength.

The thermal-hydro mechanical characteristics of the soil shear strength will be displayed as spatial distributions across stages of 4 km x 4 km, over a study period of 7 years. Soil strength is the primary stabilizing factor contributing to the structural reliability of the foundation for any structure. The hypothesis is that concurrent high temperatures and low volumetric moisture contents in soils will decrease the suction stress and consequently, shear strength, resulting in significant impacts on the resilience of our infrastructure and consequently, our society and economy.

Recognition of the behavior of the suction stress under extreme climatic conditions such as prolonged drought cycles can mark an important shift in adapting our infrastructure to a changing climate. Further, variations in the suction stress because of the non-montonic trend. It is noted that the suction stress under too wet (i.e., extreme rainfall), or inversely too dry (i.e., extreme drought) conditions is almost nonexistent. Such behavior can adversely impact the resilience of our critical geotechnical earthen structures.

The *hypothesis* of the future work is that the current warming trend under a changing climate dominates simultaneous variations in soil temperature and moisture leading to reductions in soil strength. The *long term research goal* of this work is to carefully understand the effects of the rate and variability of temperature and moisture under a changing climate on the short- and long-term thermo-hydro-mechanical properties of soil.

It is noted that a major effect of drought is shrinkage cracking, which can extend to a considerable depth. The cracks allow rapid access of water to the soil at depth under rates not achievable for intact soil. Moreover, the surface of the cracks readily soften, thus reducing the strength of the soil mass, even if the bulk of the intact soil between cracks remains dry. It follows that to really get at the problem of drought on the structural integrity of slopes in the face of large precipitation events there must be a means to analyze cracked soil masses. All of the models presented here are for intact soil. Using intact soil properties, the rate of infiltration may be underestimated, the softening caused by re-saturation can be incorrectly displayed, and the internal water forces will be under-estimated. Therefore, it is recommended that the effects of dessication cracking on soil strength be included in the list of items to study and understand.

REFERENCES


Aghakouchak, A., Feldman, D., Stewardson, M., Saphores, J., Grant, S., and Sanders, B. (2014a). "Australia's Drought: Lessons for California." *Science*, 343, 1430.

AghaKouchak, A., Cheng, L., Mazdiyasni, O., Farahmand, A. (2014b). "Global Warming and Changes in Risk of Concurrent Climate Extremes: Insights from the 2014 California Drought", *Geophysical Research Letters*, 41, 8847-8852, doi: 10.1002/2014GL062308.

AghaKouchak A., Feldman D., Hoerling M., Huxman T., Lund J., (2015), Recognize Anthropogenic Drought, *Nature*, 524 (7566), 409-4011.

ASCE. (2015). *Adapting infrastructure and civil engineering practice to a changing climate*, American Society of Civil Engineers, http://ascelibrary.org/doi/pdf/10.1061/ 9780784479193.

Baram, S., Ronen, Z., Kurtzman, D., Külls, C., and Dahan, O. (2013). "Desiccation-crack-induced salinization in deep clay sediment." Hydrology Earth System Science, 17, 1533–1545.

Bishop, A. W. (1959). "The principle of effective stress." *Tek. Ukeblad,* 106(39), 859–863.

Bittelli, M., Ventura, F., Campbell, G. S., Snyder, R. L., Gallegati, F., & Pisa, P. R. (2008). "Coupling of heat, water vapor, and liquid water fluxes to compute evaporation in bare soils." *Journal of Hydrology*, 362(3), 191-205.

Bonnin, G.M., Martin, D., Lin, B., Parzybok, T., Yekta, M., and Riley, D. (2006). "Precipitation-frequency atlas of the United States." *NOAA Atlas 14*, 1 – 64.

Briaud, J., Chen, H., Govindasamy, A., and Storesund, R. (2008). "Levee Erosion by Overtopping in New Orleans during the Katrina Hurricane." J. Geotech. Geoenviron. Eng. 134, SPECIAL ISSUE: Performance of Geo-Systems during Hurricane Katrina, 618–632.

Brooks, B.A., G. Bawden, D. Manjunath, C. Werner, N. Knowles, J. Foster, J. Dudas, and D.R. Cayan. (2012). "Contemporaneous subsidence and levee overtopping potential, Sacramento-San Joaquin Delta, California." *San Francisco Estuary and Watershed Science*, 10(1).

Buck, A. L. (1981). New equations for computing vapor pressure and enhancement factor. *Journal of applied meteorology*, 20(12), 1527-1532.

Campbell, G.S., Jungbauer, J.D., Bidlake, W.R., Hungerford, R.D. (1988). "Predicting the effect of temperature on soil thermal conductivity." *Soil Sci*. 158, 307–313.

Cascini, L., Cuomo, S., Pastor, M., and Sorbino, G. (2010). "Modeling of Rainfall-Induced Shallow Landslides of the Flow-Type." *J. Geotech. Geoenviron. Eng.*, 136(1), 85–98.

Cass, A., Campbell, G.S., Jones, T.L. (1984). "Enhancement of thermal water vapor diffusion in soil." *Soil Sci. Soc. Am.* J. 48, 25–32.

CERTO.io. (2015). "What happened during the last El Niño?" Retrieve on September 16, 2015 from cert.io.com: http://cert.io/what-happened-during-the-last-el-nino/.

CDWR. (2011). *Flood Control System Status Report*, Central Valley Flood Management Planning (CVFMP) Program, California Department of Water Resources, State of California, December 2011. http://www.water.ca.gov/cvfmp/docs/FCSSRDec2011 _FullDocument.pdf.

Cheng, L. and AghaKouchak, A. (2014). "Nonstationary precipitation Intensity-Duration-Frequency curves for infrastructure design in a changing climate." *Scientific Reports*, 10.1038/srep07093, 7093.

Cheng L., AghaKouchak, A., Gilleland, E., and Katz, R.W. (2014). "Nonstationary Extreme Value Analysis in a Changing Climate", *Climatic Change*, 127(2), 353-369.

Coe, J.A., & Godt, J.W. (2012). Review of approaches for assessing the impact of climate change on landslide hazards, In: Landslides and Engineered Slopes, Protecting Society Through Improved Understanding, *Proceedings of the 11th International and 2nd North American Symposium on Landslides and Engineered Slopes*, E. Eberhardt, C. Froese, A.K. Turner & S. Leroueil, eds.. Banff, Canada, 3-8 June 2012, Taylor & Francis Group, London, v. 1, 371-377.

Coles, S., Bawa, J., Trenner, L. and Dorazio, P. (2001). *An introduction to statistical modeling of extreme values*, Springer, London.

Crozier, M. J., (2010). "Deciphering the effect of climate change on landslide activity: a review." *Geomorphology*, 124, 260–267.

Cruden, D. M., and D. J. Varnes. (1996). "Landslide types and processes, in Landslides: Investigation and Mitigation, Transportation Research Board Special Report", 247, 36–75, edited by A. K. Turner and R. L. Schuster, *Natl. Acad. Press*, Washington, D.C.

Davidson, E., Samanta, S., Caramori, S. and Savage, K. (2012). "The dual Arrhenius and Michaelis–Menten kinetics model for decomposition of soil organic matter at hourly to seasonal time scales", *Global Change Biol*., 18(1), 371–384.

Deverel, S.J., and Leighton, D.A. (2010). "Historic, recent, and future subsidence, Sacramento-San Joaquin Delta, California, USA." *San Francisco Estuary and Watershed Science*, 8(2), http://escholarship.org/uc/item/7xd4x0xw.

de Vries, D.A. (1963). "Thermal properties in soil." In: van Wijk, W.R. (Ed.), *Physics of Plant Environment*. North Holland Pub. Co., Amsterdam, pp. 210–235.

Dixon, T.H., Amelung, F., Ferretti, A., Novali, F., Rocca, F., Dokka, R., Sella, G., Kim, S.W., Wdowinski, S., and Whitman, D. (2006). "Subsidence and flooding in New Orleans." *Nature*, 441, 587-588.

Doorenbos, J. and W.O., Pruitt. (1977). "Guidelines for predicting crop water requirements." FAO Irrigation Paper No. 24, 2nd ed., *Food and Agriculture Organization of the United Nations*, Rome, Italy, pp. 1-107.

Dunbar, J., Llopis, J., Sills, G., Smith, E., Miller, R., Ivanov, J., and Corwin, R. (2007). "Condition Assessment of Levees, U.S. Section of the International Boundary and Water Commission." *Technical Report No. TR-03-4*, U.S. Army Engineer Geotechnical and Structures Laboratory, Vicksburg, MS, pp. 332.

Dyer, M.R., Utili, S., Zielinski,. M. (2009). "Field survey of desiccation fissuring of flood embankments." *Water Management*, 162(3), 221–232.

Farahmand A., AghaKouchak A. (2013). "A Satellite-Based Global Landslide Model", *Natural Hazards and Earth System Sciences*, 13, 1259-1267, doi:10.5194/nhess-13-1259-2013.

Fayer, M. J. (2000). "UNSAT-H version 3.0: Unsaturated soil water and heat flow model. Theory, user manual, and examples." *Pacific Northwest National Laboratory*, 13249.

Fredlund, D. G. and Rahardjo, H. (1993). *Soil Mechanics for Unsaturated Soils*, John Wiley & Sons, Inc., New York, 517 pp.

Fredlund, D. G., Rahardjo, H., & Fredlund, M. D. (2012). *Unsaturated soil mechanics in engineering practice*. John Wiley & Sons.

Fredlund, D. G., & Vanapalli, S. K. (2002). *2.7 Shear Strength of Unsaturated Soils*. Methods of Soil Analysis: Part 4 Physical Methods, (methodsofsoilan4), 329-361.

Gregersen, I. B., Madsen, H., Rosbjerg, D. and Arnbjerg-Nielsen, K. (2013). "A spatial and non – stationary model for the frequency of extreme rainfall events." *Water Resour Res*, 49(1), 127–136.

Griffiths, D. V., and Lu, N. (2005). "Unsaturated slope stability analysis with steady infiltration or evaporation using elasto-plastic finite elements." *Int. J. Numer. Analyt. Meth. Geomech.*, 29(3), 249-267.

Hanak, E. and Lund, J. (2012). "Adapting California's water management to climate change." *Climate Change*, 111, 17 – 44.

Hao, Z., AghaKouchak, A., Nakhjiri, N., Farahmand, A. (2014). "Global Integrated Drought Monitoring and Prediction System", *Scientific Data*, 1:140001, 1-10, doi: 10.1038/sdata.2014.1.

Henderson-Sellers, B. (1984). "A new formula for latent heat of vaporization of water as a function of temperature." *Quarterly Journal of the Royal Meteorological Society*, 110(466), 1186-1190.

Hubble, T., and De Carli, E. (2015). "Mechanisms and Processes of the Millennium Drought River Bank Failures: Lower Murray River, South Australia", *Goyder Institute for Water Research Technical Report Series* No. 15/5, Adelaide, South Australia.

Iverson, R.M., George, D.L., Allstadt, K., Reid, M.E., Collins, B.D., Vallance, J.W., Schilling, S.P., Godt, J.W., Cannon, C.M., Magirl, C.S., Baum, R.L., Coe, J.A., Schulz, W.H., and Bower, J.B. (2015). "Landslide mobility and hazards: implications of the 2014 Oso disaster." *Earth and Planetary Sci Letters,* 412, 197 – 208.

Keaton, J.R., Anderson, S., Benoit, J., deLaChapelle, J., Gilbert, R., and Montgomery, D.R. (2014). "The 22 March 2014 Oso Landslide, Snohomish Country, Washington." *GEER Association Report No. GEER – 036*.

Kimball, B. A., Jackson, R. D., Nakayama, F. S., Idso, S. B., & Reginato, R. J. (1976). "Soil-heat flux determination: Temperature gradient method with computed thermal conductivities." *Soil Science Society of America Journal*, 40(1), 25-28.

KMA (2008). Report on climate change and mitigation, Korean meteorological administration, dept. of climate change response: climate change information center, (in Korea).

LAO. (2015). *Achieving State Goals for the Sacramento – San Joaquin Delta*. Sacramento: Legislative Analyst's Office.

Leshchinsky, B., Vahedifard, F., Koo, H.B., and Kim, S.H. (2015). "Yumokjeong Landslide: an investigation of progressive failure of a hillslope using the finite element method." *Landslides*, doi: 10.1007/s10346-015-0610-5.

Lu, N., & Dong, Y. (2015). "Closed-Form Equation for Thermal Conductivity of Unsaturated Soils at Room Temperature." *Journal of Geotechnical and Geoenvironmental Engineering*, 04015016.

Lu, N., and J. W. Godt (2008), Infinite slope stability under unsaturated seepage conditions, *Water Resour. Res.*, 44, W11404, doi:10.1029/2008WR006976.

Lu, N., and Godt, J. W. (2011). *Hillslope Hydrology and Stability*, Cambridge University Press, Oxford.

Lu, N., Godt, J. W., and Wu, D. T. (2010). "A closed-form equation for effective stress in unsaturated soil." *Water Resour. Res.,* 46(5), W05515.

Lu, N., & Likos, W. J. (2004). *Unsaturated soil mechanics*. Wiley.

Lu, N., & Likos, W. J. (2006). "Suction stress characteristic curve for unsaturated soil." *Journal of Geotechnical and Geoenvironmental Engineering*, 132(2), 131-142.

Lu, N., Şener, B., Wayllace, A., Godt, J.W. (2012). "Analysis of rainfall-induced slope instability using a field of local factor of safety." *Water Resour Res*, 48(9), W09524. doi:10.1029/ 2012WR01 1830.

Melchiorre, C., and Frattini, P. (2012). "Modelling probability of rainfall-induced shallow landslides in a changing climate", Otta, Central Norway. *Climatic change*, 113(2), 413-436.

Mount, J., and Twiss, R. (2005) "Subsidence, sea level rise, seismicity in the Sacramento-San Joaquin Delta." *San Francisco Estuary and Watershed Science*, 3(1), http://repositories.cdlib.org/jmie/sfews/vol3/iss1/art5.

Mualem, Y. (1976). "A new model for predicting hydraulic conductivity of unsaturated porous media." *Water Resources Research*, 12(3): 513–522.

NDL. (2013). *National Levee Database, User Manual: Public User Version 3.0*, US Army Corps of Engineers (USACE) Cold Regions Research and Engineering Laboratory (CRREL). 17 April.

NRC (2008). *Potential Impacts of Climate Change on US Transport*. Committee on Climate Change and US Transportation, Transportation Research Board, Division on Earth and Life Studies, National Research Council of the National Academies, Washington, DC, ISBN: 978-0-309-11306-9, 296 pages.

NRC. (2012). *Dam and levee safety and community resilience: A vision for future practice*. National Research Council. The National Academies Press, Washington, DC.

NRC (2013). *Abrupt Impacts of Climate Change: Anticipating Surprises*. Committee on Understanding and Monitoring Abrupt Climate Change and Its Impacts; Board on Atmospheric Sciences and Climate; Division on Earth and Life Studies; National Research Council of the National Academies, Washington, DC, ISBN: 978-0-309-28773-9, 250 pages.

Philip, J.R., de Vries, D.A. (1957). "Moisture movement in porous materials under temperature gradients." *Trans. Am. Geophys. Union* 38, 222–231.

Port, P.S. and Hoover, S. A. (2011). "Anticipating California Levee Failure: The State of the Delta Levees and Government Preparation and Response Strategies for Protecting Natural Resources from Freshwater Oil Spills." *International Oil Spill Conference Proceedings*: March 2011, 2011(1), abs112.

Prigg, M. (2015). "El Niño gets upgraded: Forecasters say there is a 95% chance of 'strong' weather system - but warn it WON'T relieve California's drought." Retrieved on September 15, 2016 from daily mail.com: http://www.dailymail.co.uk/sciencetech/article-3231402/El-Ni-o-gets-upgraded-Forecasters-say-95-chance-strong-weather-warn-WON-T-relieve-California-s-drought.html.

Rahardjo, H., Ong, T. H., Rezaur, R. B., & Leong, E. C. (2007). "Factors controlling instability of homogeneous soil slopes under rainfall." *J. Geotech. Geoenviron. Eng.*, 133(12), 1532-1543.

Reinert, E., Stewart, J. P., Moss, R. E. S., and Brandenberg, S. J. (2014). "Dynamic Response of a Model Levee on Sherman Island Peat: A Curated Data Set". *Earthquake Spectra*, 30(2), 639-656.

Robinson, J.D., Vahedifard, F. "Weakening mechanisms imposed on California's levees under multiyear extreme drought." *Climatic Change* (Under review, Submitted July 2015).

Rui, H. and Mocko, D. (2014). *North American Land Data Assimilation System Phase 2 (NLDAS-2) Products*.

Schuster, R. L. and Highland, L. (2001). *Socioeconomic and environmental impacts of landslides in the western hemisphere*. US Department of the Interior, US Geological Survey.

Shukla, S., Safeeq, M., AghaKouchak, A., Guan, K., Funk, C. (2015). "Temperature Impacts on the Water Year 2014 Drought in California", *Geophysical Research Letters*, doi: 10.1002/2015GL063666.

Sidle, R.C. (2007). "Using weather and climate information for landslide prevention and mitigation." In M.Y.K. Sivakumar & N. Ndiang'ui (eds.), *Climate and Land Degradation,* 285- 307. Berlin: Springer.

Sierra, C., Trumbore, S., Davidson, E., Vicca, S., and Janssens, I. (2015). "Sensitivity of decomposition rates of soil organic matter with respect to simultaneous changes in temperature and moisture", *J. Adv. Model. Earth Syst*., 7, 335–356, doi: 10.1002/2014MS000358.

Smith, I.M. and Griffiths, D.V. (1997). *Programming the Finite Element Method*, Third Edition, West Sussex, England: John Wiley and Sons Ltd.

Sorooshian, S., AghaKouchak, A., Arkin, P., Eylander, J., Foufoula-Georgiou, E., Harmon, R., and Skofronick-Jackson, G. (2011). "Advanced concepts on remote sensing of precipitation at multiple scales." *Bulletin of the American Meteorological Society*, 92(10).

Tang, C., Shi, B., Lui, C., Gao, L., and Inyang, H. (2011). "Experimental investigation of the desiccation cracking behavior of soil layers during drying." *J. Mat. in Civ. Eng.*, 23(6), 873–878.

Ter Braak, C. J. (2006). "A Markov Chain Monte Carlo version of the genetic algorithm Differential Evolution: easy Bayesian computing for real parameter spaces." *Stat. Comput.*, 16, 239–249.

Todd, A. (2010). "Levees crack under drought strain." News. Retrieved on June 14, 2015 from adelaidenow.com.au: http://www.adelaidenow.com.au/news/south-australia/levees-crack-under-drought-strain/story-e6frea83-1225972150006.

USGCRP. (2009). *Global Climate Change Impacts in the United States*, U.S. Global Change Research Program, Cambridge University Press, ISBN 978-0-521-14407-0.

Vahedifard, F., AghaKouchak, A., Robinson. J. D., (2015a). "Drought Threatens California's Levees." *Science*, 349(6250), 799, DOI: 10.1126/science.349.6250.799-a.

Vahedifard, F., Leshchinsky, B., Mortezaei, K., and Lu, N. (2015b). "Active earth pressures for unsaturated retaining structures." *J. Geotech. Geoenviron. Eng.*, 141(11), 04015048.

Vahedifard, F., Leshchinsky, D., Mortezaei, K., and Lu, N. (2015c). "Effective stress-based limit equilibrium analysis for homogenous unsaturated slopes." *Int. J. Geomech.*, 10.1061/(ASCE)GM.1943-5622.0000554.

Vahedifard, F., and Robinson, J. D., (2015). "A unified method for estimating the ultimate bearing capacity of shallow foundations in variably saturated soils under steady flow." *J. Geotech. Geoenviron. Eng.*, DOI: 10.1061/(ASCE)GT.1943-5606.0001445.

Vanapalli, S. K., Fredlund, D. G., Pufahl, D. E., and Clifton, A. W. (1996). "Model for the prediction of shear strength with respect to soil suction." *Can. Geotech. J.,* 33(3), 379–392.

Van Baars, S. (2004), "Peat Dike Failure in the Netherlands", *European Water Management Online*, European Water Association (EWA), Hennef, Germany, 1 – 11.

Van Baars, S. (2005). "The horizontal failure mechanism of the Wilnis peat dyke", Géotechnique, 55(4), 319-323.

Van Dijk, A., Beck, H., Russell, C., de Jeu, Richard, Liu, Y., Podger, G., Timbal, B., and Viney, N. (2013). "The Millennium Drought in southeast Australia (2001 – 2009): Natural and human causes and implications for water resources, ecosystems, economy, and society." *Water Resour. Res.*, 49, 1040 – 1057.

van Genuchten, M. T. (1980). "A closed form equation predicting the hydraulic conductivity of unsaturated soils." *Soil Sci. Soc. Am.,* 44, 892–898.

Vardon, P. (2014). "Climatic influence on geotechnical infrastructure: A review." *Env. Geotechnics*, 2(3), 166-174.

Vicuña, S., Hanemann, M., and Dale, L. (2006). "Economic Impacts of Delta Levee Failure Due to Climate Change: A Scenario Analysis." University of California, Berkeley for the California Energy Commission, PIER Energy-Related Environmental Research. CEC-500-2006-004.

Voight, B., Janda, R.J., Glicken, H., Douglas, P.M., (1983). "Nature and mechanics of the Mount St. Helens rockslide-avalanche of 18 May 1980." *Geotechnique*, 33, 243–273.

Vrugt, J. A., Braak, C.J.F., Diks, C.G.H., Robinson, B.A., Hyman, J.M., and Higdon, D. (2009). "Accelerating Markov chain Monte Carlo simulation by differential evolution with self-adaptive randomized subspace sampling. *Int J Nonlin. Sci. Num.*, 10(3), 273–290.